Effects of Inhomogeneous Ice Particle Habit Distribution on Passive Microwave Radiative Transfer Simulations

Jiseob Kim, Dong-Bin Shin, and Donghyeck Kim

***Abstract*— Accurately representing ice clouds in passive microwave radiative transfer models (RTMs) is considerably challenging as these clouds include numerous ice particles with complex shapes. Current RTMs often oversimplify this complexity by assuming spherical or singular nonspherical habits for these particles. This study improves the representation of ice clouds in RTMs, shifting from the oversimplified "one-shape-fits-all" approach to a more realistic approach describing the inhomogeneous distribution of ice habits. This improved representation is facilitated by the predicted particle properties (P3) microphysics parameterization scheme, which provides natural variability of the ice-phase hydrometeors' microphysical properties. The impact of this improved representation on microwave scattering is evaluated by comparing the simulated brightness temperatures (TBs) with actual measurements from the global precipitation measurement (GPM) microwave imager (GMI) at scattering frequencies between 89 and 183 GHz, mainly focusing on tropical cyclone events in the Northwestern Pacific Ocean. The results show that the improved representation effectively describes the spatiotemporal variability of ice habits, improving the accuracy of TB simulations across the scattering channels. Moreover, investigations are conducted till the frequency of 664 GHz, emphasizing the potential importance of realistic ice habit distribution. Although some limitations exist, primarily relating to the model's dependence on the P3 scheme and the limited range of the available ice habits, especially for rimed particles, this study takes a significant step toward improving the realism and accuracy of RTMs, providing a deeper understanding of ice clouds and their influence on RTMs.**

***Index Terms*— Microphysics properties, nonspherical ice particles, optical scattering, passive microwave radiative transfer model (RTM).**

I. Introduction

CLOUDS are fundamental components of the Earth's hydrological cycle and significantly influence the planet's energy balance and atmospheric circulation. To predict weather and climate patterns, cloud behavior needs to be comprehensively understood. However, the complex microphysical properties of hydrometeors, such as hydrometeor species, particle size distributions (PSDs), mass–diameter (m–D) relationships, and particle shapes, are the least understood elements in weather and climate models, as noted by Klein et al. [1], Forbes et al. [2], and Geer [3]. Satellite-based passive microwave radiometers have been widely used to explore these cloud properties and their impact on weather, climate, and the hydrological cycle. Using microwaves that can penetrate clouds, these radiometers measure brightness temperatures (TBs) at the top-of-atmosphere. When a radiation beam traverses the cloud, it is absorbed, emitted, or scattered by suspended particles (e.g., liquid water droplets and ice particles), substantially changing the TBs. This enables: 1) the quantification of the cloud properties, as shown in [4], and 2) assimilation of the cloud-influenced radiometric information, subsequently increasing the accuracy of numerical weather forecasts, as evidenced by studies from Geer et al. [5], [6], [7]. In these processes, radiative transfer models (RTMs) serve as a critical tool connecting the cloud information with the corresponding radiometric observations.

The use of passive microwave RTMs began with the launch of the first passive microwave radiometer onboard the Nimbus-5 satellite: the Electrically Scanning Microwave Radiometer (ESMR). According to Wilheit et al. [8], an early version of the RTM was primarily designed to simulate horizontally uniform layers of liquid hydrometeors. Subsequent studies by Weinman and Davies [9] and Wilheit et al. [10] included frozen hydrometeors. Later studies, including Mugnai and Smith [11], Adler et al. [12], and Smith et al. [13], made the representation of the hydrometeor distributions more realistic although their microphysical assumptions are only appropriate for specific cloud systems (e.g., convective storms). Skofronick-Jackson et al. [14] demonstrated that simulated TBs are considerably sensitive to microphysical assumptions. Thereafter, numerous researchers, including Doherty et al. [15], Matsui et al. [16], [17], Shi et al. [18], and Han et al. [19], [20], have attempted to minimize the uncertainties in their RTMs by making diverse microphysical assumptions.

The accurate computation of the scattering properties stemming from the intricate nature of ice particles is a substantial challenge faced by current RTMs. Ice particles have a wider range of species, sizes, and densities than liquid water droplets. The complexity further increases when considering the shape (or habit) distributions of the ice particles, as most ice particles in the natural atmosphere comprise combinations of different shapes, as reported in [21], [22], [23], and [24]. Hence, for simplicity, ice particles have generally been assumed to be spherical, employing the Mie scattering code as implemented by Bauer [25] for the computation of the scattering properties (e.g., [15], [16], [17], [18], [19], [20], [26]). However, several

Manuscript received 31 August 2023; revised 24 November 2023 and 27 December 2023; accepted 30 December 2023. Date of publication 3 January 2024; date of current version 17 January 2024. This work was supported by the National Research Foundation of Korea (NRF) grant funded by the Ministry of Science, ICT and Future Planning (MSIP) under Grant NRF-2023R1A2C100486011. *(Corresponding author: Dong-Bin Shin.)*

The authors are with the Department of Atmospheric Sciences, Yonsei University, Seoul 03722, South Korea (e-mail: dbshin@yonsei.ac.kr).

Digital Object Identifier 10.1109/TGRS.2024.3349484

studies, including [27], [28], [29], [30], and [31], have indicated that the spherical assumption for nonspherical particles leads to several disadvantages, such as significant warm biases of TBs at frequencies exceeding 100 GHz. To avoid these disadvantages, the discrete-dipole approximation (DDA) [32], [33] method is recommended for nonspherical particles in the microwave range.

However, the simulation of the microwave scattering by nonspherical particles is still simplified and unrealistic. Currently, RTMs commonly represent ice particles as either spherical or singular nonspherical habits per category. For example, the radiative transfer for TOVS (RTTOV; [34]) version 13.0 uses the *Large Plate Aggregate* for snow, *Column* for graupel, and *Large Column Aggregate* for ice cloud (refer to [7]), while the community RTM (CRTM) [35] and [36] version 2.4.1 uses the *Sector Snowflake* for snow and *Sphere* for other categories (refer to [37]). This oversimplified "one-shape-fits-all" assumption fails to capture the inherent complexity of the ice particle shape distributions within clouds, as mentioned in [3] and [38].

The concept of employing an ensemble of ice particle habits to refine simulations has been explored in previous studies, though often in the context of solar and near-infrared rather than microwave radiance. For instance, McFarquhar et al. [39] assumed an ensemble of *Spheres*, *Hexagonal Ice Columns*, *Bullet-Rosettes*, and *Polycrystals* to simulate solar and near-infrared reflectances in cirrus clouds. Subsequent work by Rolland et al. [40], McFarquhar et al. [41], Baum et al. [42], and Baran and Labonnote [43] further underscored the significance of the ensemble approach demonstrating that mixed habits provided a better representation of cirrus bulk properties than single habits. However, such studies in the microwave spectrum are more challenging and have been less frequently conducted. Kulie et al. [27] employed a fixed ensemble of ice particle habits, albeit without a physical basis or adaptability. More recently, Barreyat et al. [44] advanced this approach by using an adaptive ensemble of ice particle habits, though still lacking a physical underpinning. Our study extends these efforts by employing an ensemble that adapts dynamically and aligns physically with cloud microphysical processes, enhancing the simulation fidelity. This improvement is realized by constructing combinations of various ice habits, taking advantage of the flexible microphysical properties of the predicted particle properties (P3) microphysics parameterization scheme of Morrison and Milbrandt [45].

To evaluate the effects of inhomogeneous ice habit distributions on the radiance, simulated TBs are compared with observed TBs from the global precipitation measurement (GPM) microwave imager (GMI) instrument at scattering frequencies between 89 and 183 GHz, primarily focusing on tropical cyclone events in the Northwestern Pacific Ocean. In addition, this study extends the observations to the scattering frequency of 664 GHz, exploring how this high frequency interacts with different ice habits.

This article is organized as follows. Section II introduces the employed models, focusing on their key components. Section III describes the methodology for calculating the scattering properties considering the improved representation of ice clouds. Section IV provides the effects of these properties on TBs during tropical cyclone events. Finally, Section V provides the conclusions.

II. Model Descriptions

A. Passive Microwave RTM

Passive microwave RTMs are employed to simulate the propagation of microwave radiation through the atmosphere and its interaction with various components, such as gases and cloud particles. They calculate the observed radiance (i.e., TB) through a passive microwave radiometer on a satellite. Generally, RTMs comprise four submodels: surface emissivity model, atmospheric transmittance model, extinction and scattering model (hereinafter, the "scattering model"), and solver for the radiative transfer equation.

The surface emissivity model describes the relationship between microwave radiation and the surface's physical properties. To focus on cloud–radiation interactions, this study restricts the surface type to relatively uniform ocean surfaces. Therefore, the FAST microwave Emissivity Model version 6 (FASTEM-6) [46] is employed. The atmospheric transmittance model describes the interaction between microwave radiation and absorbing gases (i.e., O_2, H_2O, and N_2). The millimeter-wave propagation model (MPM93), developed by Liebe et al. [47], is used as the atmospheric transmittance model. The scattering model calculates the absorption, scattering, and extinction of radiation by cloud particles. In the microwave region, these optical properties are commonly determined using two models: the Mie and DDA scattering calculations. The Mie theory provides an analytical solution for Maxwell's equations, but it is applicable only to homogeneous spherical particles. DDA enables the accurate computation of the optical properties of nonspherical particles. Herein, both Mie and DDA scattering calculations are utilized to account for the scattering effect caused by various ice habits. Further details are provided in Section II-B. The determined optical properties are used to solve the radiative transfer equation. The delta-Eddington approximation (e.g., [48], [49]) is used to solve the radiative transfer equation for a plane-parallel two-stream atmosphere.

In addition, the average cloud fraction, proposed by Geer et al. [50], is used to capture the subgrid-scale variability of the water content in the model grid box. The refractive index of Mätzler [51] applies to both liquid and ice particles. To maintain computational efficiency, the proposed RTM is designed to be a fast model, and therefore, all particles are assumed to be spherical or randomly oriented. However, this assumption does not theoretically account for the polarization differences induced by nonspherical particles, especially in high-frequency channels above 80 GHz. Therefore, the polarization difference correction, proposed by Barlakas et al. [52], is applied to the relevant channels. Finally, all the TBs simulated by the RTM are coupled with the viewing geometry and channel specifications of the GPM GMI sensor (refer to [53]). Then, they are collocated with each channel's field of view (FOV) location.

B. Scattering Model

In passive microwave RTMs, the scattering model determines the optical properties of hydrometeors, such as liquid water droplets and ice particles. Single-scattering properties, such as absorption efficiency (Q_{abs}), scattering efficiency (Q_{sca}), extinction efficiency ($Q_{\text{ext}} = Q_{\text{abs}} + Q_{\text{sca}}$), and scattering phase matrix ($\hat{P}$), describe how a particle interacts with light. The absorption, scattering, and extinction efficiencies are defined as the ratio of the absorption, scattering, and extinction cross section (σ) to the geometric cross section of the particle, respectively,

$$Q = \frac{4\sigma}{\pi D^2} \tag{1}$$

where D represents the particle's geometric diameter, which is defined as either the maximum dimension or the volume equivalent diameter. This study adopts the maximum dimension of the particle as the diameter, following the approach of Geer et al. [7]. The cross sections depend on the refractive index and the size parameter ($x = \pi D/\Lambda$), where Λ is the wavelength of the light. In addition, the scattering phase matrix ($\hat{P}$) describes the shift in the phase of the light waves after scattering by the particles. Specifically, the first element (P_{11}), known as the scattering phase function, describes the intensity of scattered light as a function of the scattering angle. The other matrix elements comprise information about the polarization of the scattered light. When particles are spherical or randomly oriented, these other matrix elements can be neglected, which simplifies the calculations, as described by Bohren and Huffman [54].

This study uses the Mie scattering model to determine the single-scattering properties of cloud water, rain, and spherical ice particles. When considering homogeneous mixtures of ice and air, the refractive index is calibrated using the Maxwell–Garnett mixing rule (air in ice), as proposed by Garnett [55]. In such cases, the inhomogeneous effects arising from the particle's internal structure are disregarded, as they negligibly affect the realistic ice particle sizes, according to Tang et al. [56]. However, Mie scattering can lead to significant errors for nonspherical particles due to its inadequate representation of both the particle shape and dielectric constant, as mentioned in [57]. Recently, many studies, including [27], [28], [29], [30], and [31], have investigated the possible errors associated with Mie scattering and have shown that Mie scattering tends to overestimate the forward scattering from ice particles, resulting in an underestimation of the scattering reduction of radiation.

To obtain the single-scattering properties of nonspherical particles, this study utilizes the DDA scattering database. However, the data for the microwave regions are limited in publicly available DDA databases (e.g., [28], [58], [59], [60]). The databases provide different single-scattering properties for various ice habits. Among the available databases, the Atmospheric Radiative Transfer Simulator (ARTS) database, created by Eriksson et al. [60], offers the most comprehensive range of single-scattering properties for various ice habits. Hence, this study employs the ARTS scattering database, which provides the extinction matrix, the absorption vector, and the phase matrix for frequencies ranging from 1 to 886.4 GHz and temperatures of 190 K, 230 K, and 270 K. Furthermore, the database covers 18 single crystals, 13 aggregates, and three rimed particles. Their visualizations can be found in Eriksson et al. [60]. The current database version assumes that all particles are randomly oriented. A newer version, introduced by Brath et al. [61], provides the single-scattering properties of oriented ice particles, but it is not used herein as it requires complex calculations. In addition, the ARTS database adopts the refractive index proposed by Mätzler [51], which aligns with the RTM settings of this study. The database and its associated interface are publicly accessible via Zenodo, a multidisciplinary open repository operated by the European Council for Nuclear Research (CERN) and the Open Access Infrastructure for Research in Europe (OpenAIRE) with the doi: https://doi.org/10.5281/zenodo.1175573.

The different ice habits have distinct m–D relationships, which can be described using a power law expression

$$m_{\text{habit}}(D) \approx \alpha_{\text{habit}} D^{\beta_{\text{habit}}} \tag{2}$$

where $m_{\text{habit}}(D)$ is the mass distribution of the ice habit. The coefficients (α_{habit} and β_{habit}) are determined through an empirical fitting of the logarithm of m_{habit} and D of particles larger than 0.2 mm (refer to [60]). In DDA calculations, $m_{\text{habit}}(D)$ is used instead of the right term in (2). Table I provides the parameters for the ice habits considered in this study. The habit names are written in italics to facilitate recognition. The particle diameter range varies depending on the ice habits, and certain habits do not cover particles smaller than 0.1 mm. To describe the smaller particles, combining these habits with others is recommended. This combination, denoted by an asterisk, is based on previous research such as [62] and [63] and the continuity of two habits. Notably, an observational study by Schmitt and Heymsfield [64] found that ice particles with a maximum dimension greater than 0.15 mm predominantly take the form of aggregates. Consequently, single crystals are excluded from this size range.

Once the single-scattering properties are determined, the bulk-scattering properties, such as the extinction coefficient (K_{ext}), scattering coefficient (K_{sca}), and asymmetry parameter (g), are calculated by combining the single-scattering properties of individual particles with the size distribution of particles over a specified diameter range ($D_{\min}$ to $D_{\max}$)

$$K_{\text{ext}} = \int_{D_{\min}}^{D_{\max}} \sigma_{\text{ext}}(D) N(D) dD \tag{3}$$

$$K_{\text{sca}} = \int_{D_{\min}}^{D_{\max}} \sigma_{\text{sca}}(D) N(D) dD \tag{4}$$

$$g = \frac{1}{K_{\text{sca}}} \int_{D_{\min}}^{D_{\max}} \frac{1}{2} \int_0^{\pi} P_{11}(D,\theta) \cos\theta \sin\theta d\theta \sigma_{\text{sca}}(D) N(D) dD \tag{5}$$

where θ represents the angle between the incident and scattered beams. The single-scattering albedo (SSA; ω_0) is defined as the ratio of K_{sca} to K_{ext}. $N(D)$ is the number of particles within the diameter range from D to $D + dD$. Consequently, the scattering model relies on information about the microphysical properties of hydrometeors. This information can

TABLE I

SUMMARY OF THE ICE HABITS EMPLOYED IN THIS STUDY. THE MASS–SIZE RELATIONSHIPS ARE DESCRIBED BY A POWER LAW EQUATION OF THE FORM $m = \alpha D^{\beta}$. ASTERISKS ARE USED TO DENOTE ICE HABITS REPRESENTING A COMBINATION OF TWO HABITS, SPECIFICALLY FOR INCLUDING A PARTICLE DIAMETER RANGE SMALLER THAN 0.1 MM. FOR SPHERICAL PARTICLES, BOTH SOLID SPHERE, AND SOFT SPHERE, THE SINGLE-SCATTERING PROPERTIES ARE CALCULATED USING THE MIE SCATTERING CODE, WHILE THE PROPERTIES OF NONSPHERICAL PARTICLES ARE OBTAINED FROM THE ARTS DATABASE [60]

ID	Ice habits		D [mm]	α_{habit} [kg/m$^{\beta}$]	β_{habit}
1	*Solid Sphere*		0.001–50	480	3.00
2	*Soft Sphere*		0.001–50	$(\pi\rho)/6$	3.00
3	*Evans Snow Aggregate*		0.032–11.755	0.20	2.39
4	*8-Column Aggregate*		0.019–9.714	65	3.00
5	*Large Column Aggregate**	*Long Column*	0.024–4.835	34	3.00
		Large Column Aggregate	0.368–19.981	0.25	2.43
6	*Large Plate Aggregate**	*Thick Plate*	0.016–3.246	110	3.00
		Large Plate Aggregate	0.349–22.860	0.21	2.26
7	*Large Block Aggregate**	*Block Column*	0.013–2.632	210	3.00
		Large Block Aggregate	0.349–21.875	0.35	2.27
8	*Spherical Graupel**	*Block Column*	0.013–2.632	210	3.00
		Spherical Graupel	0.622–9.744	13	2.69
9	*ICON Snow**	*Sector Snowflake*	0.02–12	0.00081	1.44
		ICON Snow	0.12–20	0.031	1.95
10	*GEM Snow**	*8-Column Aggregate*	0.019–9.714	65	3.00
		GEM Snow	0.17–10.459	24	2.86

be determined with microphysics parameterization schemes, which are key components of numerical weather prediction (NWP) models.

C. Convection-Permitting Model

A convection-permitting model (CPM) is a type of NWP model designed to simulate atmospheric processes at high spatial resolutions (i.e., less than 4 km). This fine resolution enables the model to explicitly represent convective processes occurring on a small scale, thereby enhancing the accuracy of the detailed predictions for severe weather events. CPM includes sophisticated parameterizations of atmospheric physics, such as the effects of radiation, turbulence, and cloud microphysics. The CPM output products (i.e., environmental and hydrometeor variables) can be used as a priori information for the radiative transfer simulations.

In this study, the weather research and forecasting (WRF) model version 4.1.5 is employed. The initial and boundary conditions are obtained from the National Centers for Environmental Prediction (NCEP) Final (FNL) dataset, with a grid resolution of 1.0° and a temporal interval of 6 h. The WRF model is configured with three domains, with horizontal resolutions of 36, 12, and 4 km, respectively. Moreover, the model utilizes 35 vertical levels up to a 50-hPa pressure top and has a fixed time step of 180 s for integration. The physics parameterizations used are given as follows: the rapid RTM (RRTM) [65] longwave radiation scheme, the Kain–Fritsch cumulus scheme proposed by Kain and Fritsch [66] (turned off for the third domain), the Yonsei University (YSU) [67] surface and planetary boundary layer (PBL) scheme, and the P3 microphysics parameterization scheme.

D. P3 Microphysics Parameterization Scheme

The P3 scheme simulates the microphysical processes of hydrometeors. It is based on a bulk microphysics approach, representing hydrometeor distributions through a few prognostic variables. However, instead of using predefined ice-phase types (e.g., cloud ice, snow, and graupel), the P3 scheme predicts the continuous evolution of a single "free" ice-phase category. It predicts four prognostic variables, i.e., ice mass mixing ratio (q_i), ice total number concentration ($N_{\text{tot},i}$), rime mass mixing ratio (q_{rime}), and rime volume mixing ratio (B_{rime}), and then uses them to diagnose the microphysical

TABLE II

m–D Relationships and Particle Densities for the P3 Ice–phase Categories. Boundaries Between Small, Unrimed, Completely Rimed, and Partially Rimed Crystals Are Defined as D_{th}, D_{gr}, and, D_{cr}, Respectively

Ice-phase category	α_{p3} [kg/m$^{\beta}$]	β_{p3}	Density [kg/m^3]	Upper threshold [m]
Small crystal	$(\pi\rho_i)/6$	3	$\rho_i = 917$	$D_{th} = (\frac{\pi\rho_i}{6\alpha_{va}})^{1/(\beta_{va}-3)}$
Unrimed crystal	$\alpha_{va} = 0.0121$	$\beta_{va} = 1.9$	$\frac{6\alpha_{va}}{\pi} D^{\beta_{va}-3}$	$D_{gr} = (\frac{6\alpha_{va}}{\pi\rho_g})^{1/(3-\beta_{va})}$
Completely rimed crystal	$(\pi\rho_g)/6$	3	ρ_g	$D_{cr} = [(\frac{1}{1-F_{rime}}) \cdot \frac{6\alpha_{va}}{\pi\rho_g}]^{1/(3-\beta_{va})}$
Partially rimed crystal	$(\frac{\alpha_{va}}{1-F_{rime}})$	β_{va}	$\frac{6\alpha_{va}}{\pi(1-F_{rime})} D^{\beta_{va}-3}$	-

properties of the ice particles, such as their m–D relationship and PSD.

The P3 scheme can depict the natural transition of ice-phase categories from unrimed to rimed crystals (e.g., small, unrimed, completely rimed, and partially rimed crystals), determining the mass distribution $m_{p3}(D)$ based on two coefficients (α_{p3} and β_{p3}), which depend on the rime fraction ($F_{\text{rime}} = q_{\text{rime}}/q_i$) and rime mass density ($\rho_{\text{rime}} = q_{\text{rime}}/B_{\text{rime}}$). Table II illustrates the m–D relationships and densities of the ice crystals obtained using the P3 scheme. For small crystals, α_{p3} is determined by the ice density ($\rho_i = 917\text{kg/m}^3$), while β_{p3} is equal to 3. The coefficients for unrimed crystals, which are grown through vapor diffusion or aggregation, are α_{va} and β_{va}, as proposed by Brown and Francis [68] and modified by Hogan et al. [69]. For partially rimed crystals, resulting from riming, α_{p3} is similar to that of the unrimed crystals but is adjusted by F_{rime}. Completely rimed crystals, which are assumed to be fully encased in rime, are treated as spherical particles with a density of ρ_g

$$\rho_g = \rho_{\text{rime}} F_{\text{rime}} + (1 - F_{\text{rime}}) \frac{6\alpha_{va}\left(D_{\text{cr}}^{\beta_{va}-2} - D_{\text{gr}}^{\beta_{va}-2}\right)}{\pi(\beta_{va}-2)\left(D_{\text{cr}} - D_{\text{gr}}\right)} \quad (6)$$

where D_{gr} and D_{cr} are the critical diameters that separate unrimed, completely rimed, and partially rimed crystals, respectively. In addition, D_{th} separates small crystals from unrimed crystals. These critical diameters represent points where the mass of adjacent ice-phase categories is equal (refer to Table II). The mass distribution of the P3 scheme is flexible, meaning that it varies with time and space. In contrast, traditional category-based microphysics schemes (e.g., [70], [71]) consider fixed α and β and, thus, do not adequately capture the diverse nature of ice particles. Morrison and Milbrandt [45] stated that the P3 scheme's flexible approach, allowing for α and β adjustments, better reflects reality than the traditional approach.

In addition, the P3 scheme allows for diverse distributions of ice particle sizes through the four prognostic variables. The generalized gamma distribution form is used to describe PSD

$$N(D) = N_{0,i} D^{\mu_i} e^{-\lambda_i D} \quad (7)$$

where $N_{0,i}$, λ_i, and μ_i are the intercept, slope, and shape parameters, respectively. The relationship between λ_i and μ_i is given as follows:

$$\mu_i = 0.0019\lambda_i^{0.8} - 2 \quad (8)$$

with the constraint of $0 < \mu_i < 6$ (refer to [22]). The PSD parameters are finally determined via moment relations using a numerical iteration method. All four prognostic variables are essential in this process, with particular emphasis on the variables associated with rime as they also govern the particle density. Compared to the traditional microphysics schemes, the P3 scheme provides additional degrees of freedom, allowing for flexible ice microphysical properties. This flexibility is highly significant when trying to realistically represent hydrometeors' distribution.

The flexibility provided by the P3 microphysics scheme is crucial for reducing unrealistic assumptions within the RTM scattering processes. In this study, the microphysics of the P3 scheme is fully incorporated into the scattering model. While the microphysical assumption of liquid hydrometeors (e.g., cloud water and rain) is used in this RTM, it is not discussed in this study, as this study specifically focuses on the scattering effects of ice particles at high frequencies. Kim et al. [72] employed the P3 scheme in their passive microwave RTM, but they only used the Mie theory. In contrast, this study additionally uses scattering databases derived from the DDA method to obtain the scattering properties for nonspherical particles. Furthermore, the effects of inhomogeneous ice habit distribution on passive microwave simulations are analyzed.

III. Representation of Ice Clouds

Ice particles within natural clouds have complex shapes, as mentioned in [21], [22], [23], and [24]. The form of individual ice crystals, stemming from nucleation processes, varies depending on the temperature and supersaturation in the surrounding environment (refer to [73]). These crystals evolve into various shapes and sizes through different growth processes, such as vapor deposition, riming, and aggregation, as described in [74]. In addition, secondary ice production

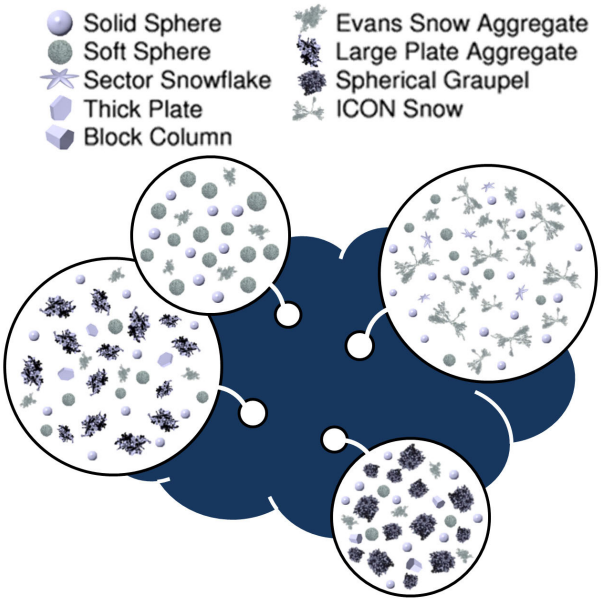

Fig. 1. Schematic illustrating the spatial inhomogeneity in the ice habit distribution within a cloud. Image of individual ice habits are sourced from the ARTS database of Eriksson et al. [60].

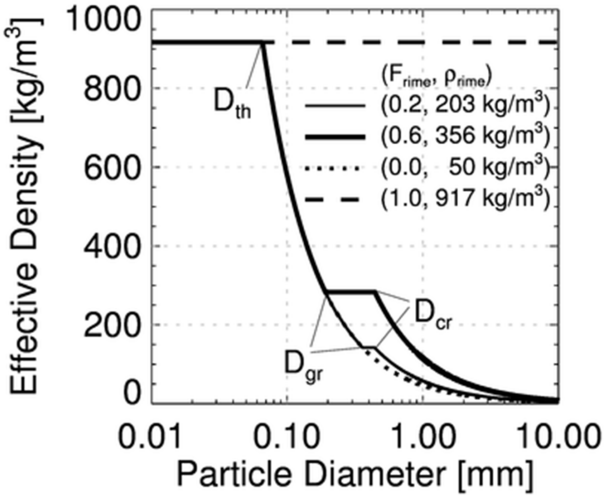

Fig. 2. P3 ice crystals' effective density as a function of the particle diameter. The different line patterns illustrate four examples of effective density, each derived from different combinations of rime fraction and density (see legend for details).

mechanisms, such as rime splintering, droplet shattering, ice–ice collisional break-up, and fragmentation, significantly increase the generation of irregular and nonspherical ice particles according to Field et al. [75]. Given this diversity, a combination of different ice habits needs to be considered to accurately determine the scattering using the RTM. Fig. 1 presents a schematic demonstrating the various mixtures of ice habits, including spheres, single crystals, aggregates, and rimed particles, as an illustrative example. This study aims to improve the representation of ice clouds, as depicted in Fig. 1, for accurate radiative transfer simulations, particularly at high microwave frequencies, which are highly sensitive to scattering by ice particles. This improvement is accomplished by constructing combinations of diverse ice habits, taking advantage of the flexible microphysical features of the P3 scheme. One of the main challenges is the selection of optimal ice habits based on physical criteria instead of solely relying on empirical considerations.

A. Optimal Ice Habit Selection

The optimal ice habit is selected using the effective density (ρ_{eff})

$$\rho_{\text{eff}} = \frac{m(D)}{\frac{\pi}{6}D^3}. \tag{9}$$

Effective density is a valuable metric that provides insights into the morphology of ice particles, as mentioned in [60], [76], and [77]. When considering perfectly spherical ice particles (i.e., *Solid Spheres*), effective density is 917kg/m^3 for all diameters. However, for spherical particles with internal voids (i.e., *Soft Spheres*), the effective density decreases below 917kg/m^3 but remains constant across different diameters. In contrast, the effective density of nonspherical particles not only decreases below 917kg/m^3 but also varies with the diameter.

Fig. 2 displays the relationship between the effective density and particle diameter within the P3 scheme. The dotted line represents the effective density of the ice particles in the absence of rimed crystals (i.e., $F_{\text{rime}} = 0$), while the dashed line represents the effective density of *Solid Spheres*. The solid lines in Fig. 2 illustrate two distinct combinations of the rime fraction and density: the thinner line corresponds to $F_{\text{rime}} = 0.2$ and $\rho_{\text{rime}} = 203$ kg/m^3, while the thicker line corresponds to $F_{\text{rime}} = 0.6$ and $\rho_{\text{rime}} = 356$kg/m^3. Additional relationships between effective density and particle diameter can be expressed depending on the combination of these two prognostic variables. As shown in Fig. 2, the effective density remains constant at 917 kg/m^3 for small crystals (i.e., $D < D_{\text{th}}$), indicating that the optimal habit for these crystals is *Solid Sphere*. In contrast, completely rimed crystals (i.e., $D_{\text{gr}} \leq D < D_{\text{cr}}$) have a lower effective density than 917 kg/m^3, indicating that the optimal habit for these crystals is close to the *Soft Sphere*. To ensure physical consistency with the P3 microphysics, both these types of crystals—the small and completely rimed ones—are considered spheres, and the Mie scattering model is employed to calculate their scattering properties. In addition, for unrimed crystals (i.e., $D_{\text{th}} \leq D < D_{\text{gr}}$) and partially rimed crystals (i.e., $D_{\text{cr}} \leq D$), the effective density decreases with increasing particle size, implying that their optimal habits are nonspherical in shape. The four types of ice crystals have different density values and display different patterns of density changes with increasing particle size.

The ARTS scattering database includes various ice habits, each characterized by its own effective density obtained by applying the given particle mass to (9). Fig. 3 provides the effective densities of the ice habits listed in Table I. For simplification, the asterisk, denoting a combined habit (refer to Table I), has been omitted. Generally, for most nonspherical ice habits, the effective density decreases with increasing

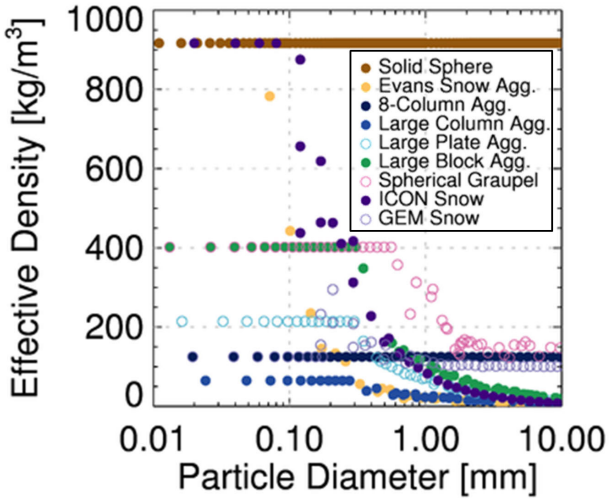

Fig. 3. Effective density plot similar to Fig. 2 but for the ice habits listed in Table I.

particle size, except for *8-Column Aggregate*, which has a constant effective density of 124.14 kg/m^3. *Spherical Graupel* has a higher effective density than other nonspherical ice habits when its diameter exceeds 0.3 mm, while the *Large Column Aggregate* has the lowest density. Furthermore, the effective density of the *Soft Sphere* is indeed not illustrated in Fig. 3.

As illustrated in Figs. 2 and 3, both the P3 ice crystals and ARTS ice habits have their respective effective densities. The root mean square error (RMSE) values of their effective densities are compared. According to the microphysical assumptions of the P3 scheme, the effective density of unrimed crystals is determined independently of the prognostic variables, such as F_{rime} and ρ_{rime} (refer to Table II). Consequently, the optimal habit for the unrimed crystals is selected independently of these variables. As depicted by the dotted line in Fig. 2, for unrimed crystals, the effective density exponentially decreases as the diameter increases beyond D_{th}. Among the ice habits listed in Table I, *Evans Snow Aggregate* (represented by yellow circles in Fig. 3) closely resembles unrimed crystals in terms of effective density, yielding the lowest RMSE value of 61.38 kg/m^3. In contrast, the other ice habits have RMSE values of 100 kg/m^3 or higher. Thus, *Evans Snow Aggregate* is the optimal habit for unrimed crystals.

In contrast to unrimed crystals, the effective density of partially rimed crystals is adjusted by F_{rime}, and its diameter boundary (D_{cr}) is determined by both F_{rime} and ρ_{rime}, as presented in Table II. Hence, the effective density of partially rimed crystals is more variable than that of unrimed crystals. To determine the optimal habit for partially rimed crystals, F_{rime} is divided into nine parts from 0.1 to 0.9 and ρ_{rime} is divided into 18 parts from 50 to 917 kg/m^3. If F_{rime} is either 0 or 1, no partially rimed crystals exist; consequently, the selection of the optimal habit is not required for such cases. Fig. 4 shows the chosen habits and their corresponding RMSE values, which are depicted through grayscale shading. Generally, *Large Plate Aggregate* (i.e., habit ID 6) is chosen as the optimal habit for partially rimed crystals when F_{rime}

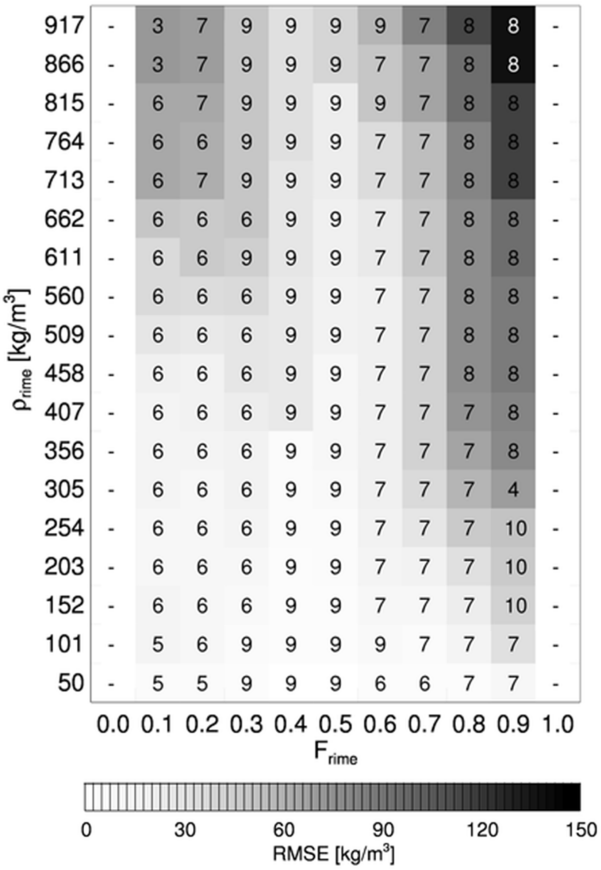

Fig. 4. Optimal ice habits for partially rimed crystals in the P3 scheme. Their ice habit ID (refer to Table I) is displayed with the corresponding RMSE value represented in grayscale. The optimal ice habits are determined by dividing F_{rime} into nine parts, ranging from 0.1 to 0.9, and ρ_{rime} into 18 parts, ranging from 50 to 917 kg/m^3.

ranges from 0.1 to 0.3, *ICON Snow* (i.e., habit ID 9) is chosen when F_{rime} ranges from 0.4 to 0.5, a *Large Block Aggregate* (i.e., habit ID 7) is chosen when F_{rime} ranges from 0.6 to 0.7, and *Spherical Graupel* (i.e., habit ID 8) is chosen when F_{rime} ranges from 0.8 to 0.9. However, when partially rimed crystals are composed of high-density rimes, the chosen habits have high RMSE values, as shown in the top right corner of Fig. 4. This problem stems from the ARTS scattering database's limited range of available ice habits, particularly for dense and strongly rimed particles, indicating a potential limitation in accurately representing these specific types of ice particles.

Consequently, the combination of F_{rime} and ρ_{rime} determines the type of ice habits and their combination status, allowing for an intricate distribution of the diverse ice habits. For instance, in a scenario where $F_{\text{rime}} = 0.2$ and $\rho_{\text{rime}} = 203\text{kg/m}^3$, the optimal ice habit is a combination of *Solid Sphere*, *Evans Snow Aggregate*, *Soft Sphere*, and *Large Plate Aggregate*. Moreover, this approach effectively describes the spatiotemporal variability of ice habits, as it relies on the prognostic variables. This approach can be applied to other microphysics schemes if they can predict the ice density. However, some discrepancies may exist in the particle masses (or effective densities), as indicated by the high RMSE values in Fig. 4. This study employs a PSD renormalization technique to minimize such differences.

B. PSD Renormalization

Geer et al. [7] proposed the PSD renormalization technique to prevent the loss or gain of total mass that results from inconsistencies in the microphysical properties. A key parameter for evaluating the degree of inconsistency in the total mass is the ice water content (IWC), denoted as l. The P3 scheme predicts the IWC, which is proportional to the βth moment (M_β) of the PSD

$$l_{p3} = \int_0^\infty m_{p3}(D)N(D)dD = \alpha_{p3} \cdot M_{\beta_{p3}}. \tag{10}$$

The scattering model reconstructs the IWC by integrating the mass of particle habits and the corresponding PSD over a given diameter range ($D_{\min}$ to $D_{\max}$) as follows:

$$l_{\text{habit}} = \int_{D_{\min}}^{D_{\max}} m_{\text{habit}}(D)N(D)dD. \tag{11}$$

This reconstructed IWC (l_{habit}) may differ from the predicted IWC (l_{p3}) due to two factors: 1) differences in particle mass and 2) deficiencies in numerical integration. The ratio of the two IWCs represents a renormalization factor (r)

$$r = \frac{l_{P3}}{l_{\text{habit}}}. \tag{12}$$

The original PSD is modified using the renormalization factor as follows:

$$N'(D) = rN(D). \tag{13}$$

The modified PSD is used in the calculation of the bulk-scattering properties in (3)–(5). This method can reduce the scattering difference caused by differences in the particle mass.

C. Inhomogeneous Distribution of Ice Habit

Fig. 5 displays the ice water path (IWP) simulated using the WRF model for the tropical cyclone "HAISHEN" at 09:20 UTC on September 3, 2020. The IWP values obtained from the simulation are collocated within the FOV of the GMI 166-GHz channel. Fig. 6 presents the vertical cross sections of the scan track indicated by the bold black line in Fig. 5. Fig. 6(a)–(c) depicts the simulated F_{rime}, simulated ρ_{rime}, and the assigned ice habits for each grid (colored rectangles) in the "HAISHEN" case, respectively. The ice habits for each grid are displayed based on the proportion of the IWC value, and a maximum of four different ice habits may be present within a single rectangle.

Fig. 6(c) effectively demonstrates the horizontal and vertical inhomogeneity of the ice habits selected through the proposed approach. Moreover, the distribution features suggest a significant association between the chosen ice habits and the ice crystal formation and growth mechanisms in clouds. In Fig. 6(a), two distinctive areas can be observed where F_{rime} exceeds 0.3. The first area is the convective core, designated by pixel numbers 12–14, 40–42, and 48–50. This area generally comprises a substantial amount of supercooled liquid water, leading to a highly efficient riming process (refer to [45]). As shown in Fig. 6(c), the ice habits in the convective core are primarily *ICON Snow* or *Large Block Aggregate*. Particularly,

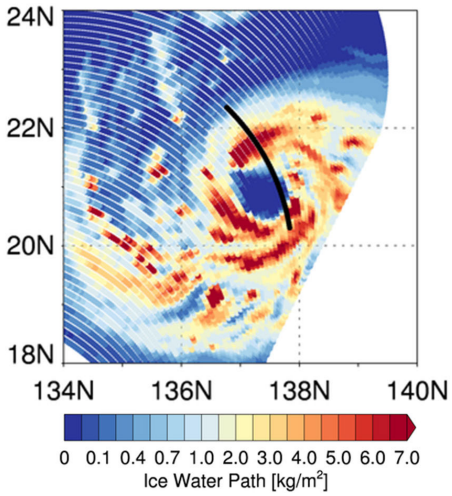

Fig. 5. IWP simulated with the WRF model using the P3 scheme for the tropical cyclone "HAISHEN" at 09:20 UTC on September 3, 2020. The solid black line represents the cross-section shown in Fig. 6.

in areas where ρ_{rime} exceeds 800kg/m^3 [see Fig. 6(b)], the ice habits are mainly *Spherical Graupel*, *Solid Sphere*, or *Soft Sphere*. These habits maintain higher effective densities, even for large particle sizes, than the other ice habits, as shown in Fig. 3. The second region is the cloud top reaching above 12 km, which has a relatively high F_{rime} despite the absence of supercooled liquid water. This is due to the horizontal transport of rimed ice crystals from convective updrafts, as described in [78]. The ice particles in this area are typically small, signifying that partially rimed crystals are less commonly found here. Hence, the *Soft Sphere* ice habit is dominant in this area. The selection of spheres as the optimal habit may seem disappointing when considering that natural ice particles are rarely perfect spheres. This choice is primarily for physical consistency with the P3 microphysics and secondary due to the limited range of rimed particles in the current ARTS database. To move toward a more realistic representation of ice particles in our methodology, advancements in both cloud microphysics schemes and DDA-based particle models are necessary.

Conversely, areas outside the convective core have F_{rime} values below 0.3 [Fig. 6(a)], implying that the primary growth mechanism is vapor deposition and aggregation (refer to [45]). *Evans Snow Aggregate* typically represents particles grown via vapor deposition and aggregation, while *Large Plate Aggregate* represents particles grown through just aggregation, as shown in Fig. 6(c).

Although the selected habits do not fully represent the shapes of ice particles formed via each growth process, they, nonetheless, share comparable effective densities. These findings indicate that the selection of the optimal ice habit is not arbitrary or empirical but relies on the fundamental physical mechanisms of crystal formation and growth in hydrometeors.

D. Bulk-Scattering Properties

The final bulk-scattering properties, encompassing all ice categories, can be expressed as the summation of integrals of the different size ranges. Each integral term utilizes the

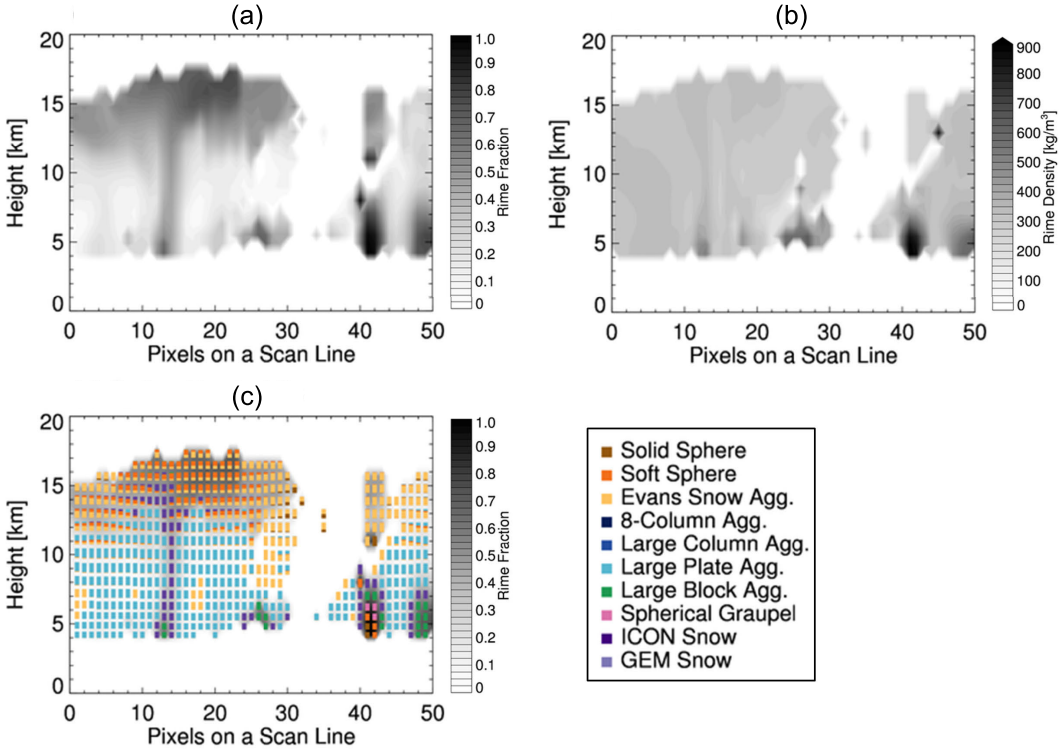

Fig. 6. Cross-sectional example of a deep convection core along the transect of interest presented in Fig. 5. (a) Rime fraction, (b) rime density, and (c) optimal ice habits overlaid on the background of the rime fraction. In (c), each grid contains up to four different ice habits (colored rectangles; see legend), and their size is proportional to the IWC for each habit.

single-scattering properties of the optimal ice habit associated with a specific ice category. For example, the extinction and scattering coefficients are

$$K = \int_{D_{\min}}^{D_{\text{th}}} \sigma_{\text{habit1}}(D)N'(D)dD + \int_{D_{\text{th}}}^{D_{\text{gr}}} \sigma_{\text{habit2}}(D)N'(D)dD + \int_{D_{\text{gr}}}^{D_{\text{cr}}} \sigma_{\text{habit3}}(D)N'(D)dD + \int_{D_{\text{cr}}}^{D_{\max}} \sigma_{\text{habit4}}(D)N'(D)dD \tag{14}$$

where $\sigma_{\text{habit\#}}$ represents the optical cross section of the optimal ice habit, which is derived from either the Mie solution or the DDA scattering database. Kim et al. [72] stated that PSD plays a crucial role in determining microwave scattering signals. They emphasized the importance of maintaining consistency between the PSD used in the scattering calculations and that of the microphysics scheme providing input profiles to the RTM. Hence, the PSD employed herein is aligned with that of the P3 scheme but is slightly adjusted via PSD renormalization.

Fig. 7 displays the bulk-scattering properties of various ice habits, including the extinction coefficient, SSA, and asymmetry parameter, along with their relative differences from the optimal ice habit, across the GMI frequency range. Note that the scattering coefficient is obtained by multiplying the extinction coefficient and SSA. The computations are performed for all combinations of the prognostic variables. However, Fig. 7 only presents two specific conditions: the top group [see Fig. 7(a)–(f)] corresponds to $F_{\text{rime}} = 0.2$ and $\rho_{\text{rime}} = 203\text{kg/m}^3$, while the bottom group [see Fig. 7(g)–(l)] corresponds to $F_{\text{rime}} = 0.6$ and $\rho_{\text{rime}} = 356\text{kg/m}^3$. In the figure, the red line represents the bulk-scattering properties obtained from the optimal ice habit, while the other colored lines depict those derived from individual ice habits.

Fig. 7 demonstrates the significant influence of the ice habits on the bulk-scattering properties. Notably, *Spherical Graupel* and *8-Column Aggregate* consistently exhibit higher extinction (scattering) coefficients relative to other habits, attributed to their higher effective densities as shown in Fig. 3. In addition, *Large Block Aggregate* and *GEM Snow* generally show higher extinction (scattering) coefficients than *Large Plate Aggregate* and *ICON Snow*. Conversely, *Evans Snow Aggregate* and *Large Column Aggregate* have lower extinction (scattering) coefficients due to their lower effective densities. The extinction (scattering) coefficients of the optimal ice habit are similar to those of *Large Plate Aggregate* at $F_{\text{rime}} = 0.2$ and $\rho_{\text{rime}} = 203\text{kg/m}^3$ and *Large Block Aggregate* at $F_{\text{rime}} = 0.6$ and $\rho_{\text{rime}} = 356\text{kg/m}^3$, respectively. This indicates that these habits are dominant within the optimal ice habit under these specific conditions.

The asymmetry parameter determines the direction of scattered radiation, ranging from pure forward scattering ($g = 1$) to complete backward scattering ($g = -1$). Generally, nonspherical particles lead to weaker forward scattering than spherical particles. In other words, the complexity of nonspherical particles' structure correlates with increases in lateral scattering, consequently resulting in a decrease in the asymmetry parameter, as mentioned in [79]. As shown in the right column of Fig 7, the asymmetry parameter of *Soft Sphere* is relatively high value. Interestingly, *GEM Snow*, despite only being quasi-spherical in appearance (refer to [80]), has

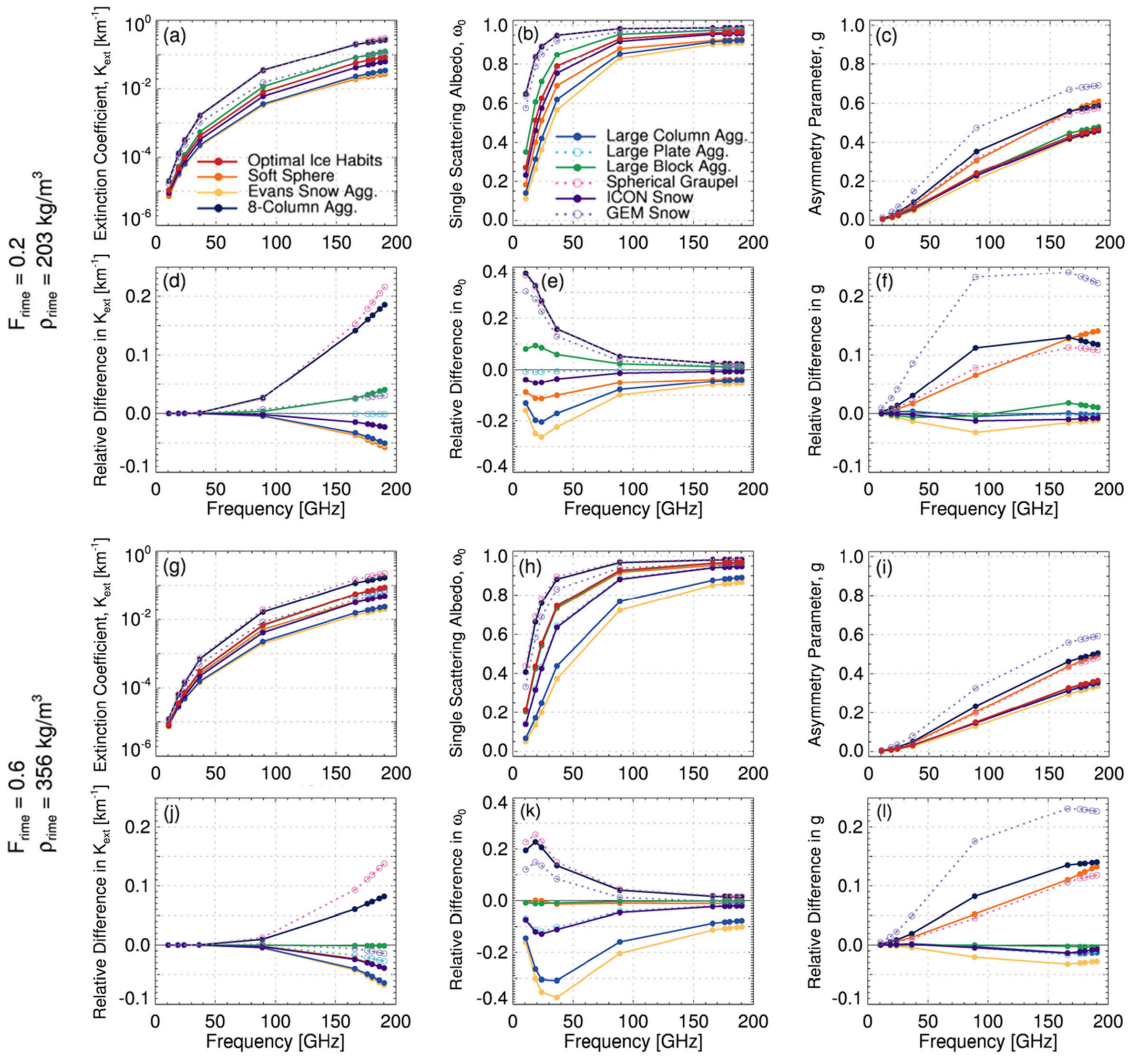

Fig. 7. Bulk-scattering properties, including (a) and (g) extinction coefficient, (b) and (h) SSA, and (c) and (i) asymmetry parameter, calculated considering the different ice habits (refer to legend) and the P3 microphysical properties. (d)–(f) and (j)–(l) Differences in the bulk-scattering properties of each ice habit relative to the optimal ice habit. Computations are performed for the IWC $l_i = 0.1$ g/m^3, ice total number concentration $N_{\text{tot},i} = 10^4\text{m}^{-3}$, and temperature $T = 246$ K for the GPM GMI frequency range (10–183 GHz). (a)–(f) Conditions with a rime fraction of 0.2 and rime density of 203kg/m^3, while (g)–(l) correspond to a rime fraction of 0.6 and rime density of 356kg/m^3.

an even higher asymmetry parameter than *Soft Sphere*. Furthermore, *8-Column Aggregate* and *Spherical Graupel* have relatively high asymmetry parameters. Owing to their high density and compactness, these particles generally have higher asymmetry parameter values, as shown in [7], contributing to increased radiation reaching the top-of-atmosphere. The calculated bulk-scattering properties are stored as a multidimensional matrix within the lookup table (LUT).

The LUT comprises various parameters such as temperatures, hydrometeor species, prognostic variables, and frequencies of the employed microwave sensors. Substantial computational resources are required to construct this multidimensional LUT, but once the LUT is generated, the RTM can run efficiently without additional burden on the processing time.

IV. Results and Discussion

A. Targeted Events

A set of specific tropical cyclones in the Northwestern Pacific Ocean during 2020 is chosen for analysis. During 2020, the considered region experienced a total of 23 tropical cyclones, and only two were not detected by the GPM GMI sensor. The sensor captured 76 observational images of 21 tropical cyclones. The information is sourced from the Japan Aerospace Exploration Agency (JAXA) Earth Observational Research Center (EORC) tropical cyclone database.

The WRF simulations are conducted over a 36-h period for tropical cyclone cases satisfying the following criteria: 1) maximum sustained wind speed exceeding 17 m/s; 2) cyclone center positioned within the GMI swath; and 3) center situated over an ocean surface. In addition, to minimize the WRF simulation errors, the allowable track and minimum sea level pressure (MSLP) errors are limited to 120 km and 20 hPa, respectively. The tropical cyclone center positions in the simulations are determined using the Geophysical Fluid Dynamics Laboratory (GFDL) vortex tracker (refer to [81]) and validated with the best track data obtained from the Joint Typhoon Warning Center (JTWC). The track and MSLP errors are primarily influenced by the model configuration like the horizontal resolution and microphysics scheme. In this study,

TABLE III

LIST OF TROPICAL CYCLONES CONSIDERED IN THIS STUDY. THEIR LOCATION AND INTENSITY DATA ARE SOURCED FROM THE JTWC BEST-TRACK DATASET. CYCLONES ARE GENERALLY CATEGORIZED INTO FOUR CLASSES BASED ON THEIR MAXIMUM WIND SPEEDS: TROPICAL DEPRESSION (TD; < 17 M/S), TROPICAL STORM (TS; 17–25 M/S), SEVERE TROPICAL STORM (STS; 25–33 M/S), AND TYPHOON (TY; ≥33 M/S). NOTE THAT MSLP REFERS TO THE MINIMUM SEA LEVEL PRESSURE AND ROCI DENOTES THE RADIUS OF THE OUTERMOST CLOSED ISOBAR

Name	Date/Time (UTC)	JTWC Best-track				
		Category	Cen. lon. [°]	Cen. lat. [°]	MSLP [hPa]	ROCI [km]
HAGUPIT	2020-08-03 05:40	TY	122.58	26.10	977.50	277.80
MAYSAK	2020-08-28 11:20	TS	129.73	16.40	996.33	506.21
	2020-08-29 21:50	TY	128.76	17.16	977.36	463.00
	2020-09-01 20:50	TY	126.69	29.92	943.25	434.71
HAISHEN	2020-09-02 20:00	TY	139.07	20.00	976.00	407.44
	2020-09-03 09:20	TY	137.09	20.77	948.89	375.54
	2020-09-05 09:10	TY	131.19	25.07	926.75	386.09
DOLPHIN	2020-09-22 03:50	STS	135.53	27.74	985.81	346.74
	2020-09-22 13:40	STS	136.21	29.52	984.39	330.79
KUJIRA	2020-09-29 01:00	STS	154.27	32.97	979.00	324.10
CHAN-HOM	2020-10-05 23:50	TS	138.64	23.87	991.11	441.91
	2020-10-07 23:30	TY	132.82	27.93	963.92	398.18
	2020-10-08 09:10	STS	133.11	29.06	966.42	370.40
SAUDEL	2020-10-21 07:20	TS	118.28	15.98	991.22	353.94
MOLAVE	2020-10-27 18:30	TY	111.18	14.24	956.67	416.70
GONI	2020-10-29 16:50	TY	133.61	16.36	953.25	262.88
ATSANI	2020-11-03 15:40	TS	129.15	19.96	1003.78	333.36
	2020-11-05 02:10	STS	126.21	20.30	997.36	311.50
VAMCO	2020-11-10 01:00	TS	128.23	13.35	1001.17	412.07

the thresholds for these errors are set by referencing the errors reported in previous studies, including [82], [83], [84], and [85]. Finally, a total of 19 scenes from 11 tropical cyclones are selected, as listed in Table III. The time difference between the WRF simulations and the GMI observations at the tropical cyclone center is kept within 5 min. The mean track error for the selected cases is calculated as 69.75 km, and the root mean square (rms) value for the MSLP errors is determined to be 8.61 hPa. The WRF simulation outputs are used as input data for the RTM to calculate the TBs at the scattering channels (including 89, 166, 183.31 ± 7, and 183.31 ± 3 GHz) of the GMI instrument.

The simulated TBs are spatially averaged to match the resolution of each channel's FOV and positioned at the center of each FOV. Only pixels within the radius of the outermost closed isobar (ROCI) of the tropical cyclones, corresponding to ocean surfaces, are selected for the analysis. Subsequently, the inclusion of clear-sky pixels, which fall outside the scope of our investigation, is reduced. Land and ocean data are acquired from the Moderate Resolution Imaging Spectroradiometer (MODIS) Land Cover Climate Modeling Grid (CMG) (MCD12C1) version 6 data products. Fig. 8 displays the GMI-observed TBs at 166-GHz V-pol for the chosen pixels. This study aims to reproduce the GMI-observed TB distribution (e.g., the left corner of Fig. 8) by improving the ice cloud representation in the scattering model.

B. TB Simulations

In this section, the scattering effects of the optimal ice habit are analyzed by comparing the simulated TBs with the observed TBs at the scattering channels. Scattering efficiency increases as the frequency increases from 89 to 183.31 GHz,

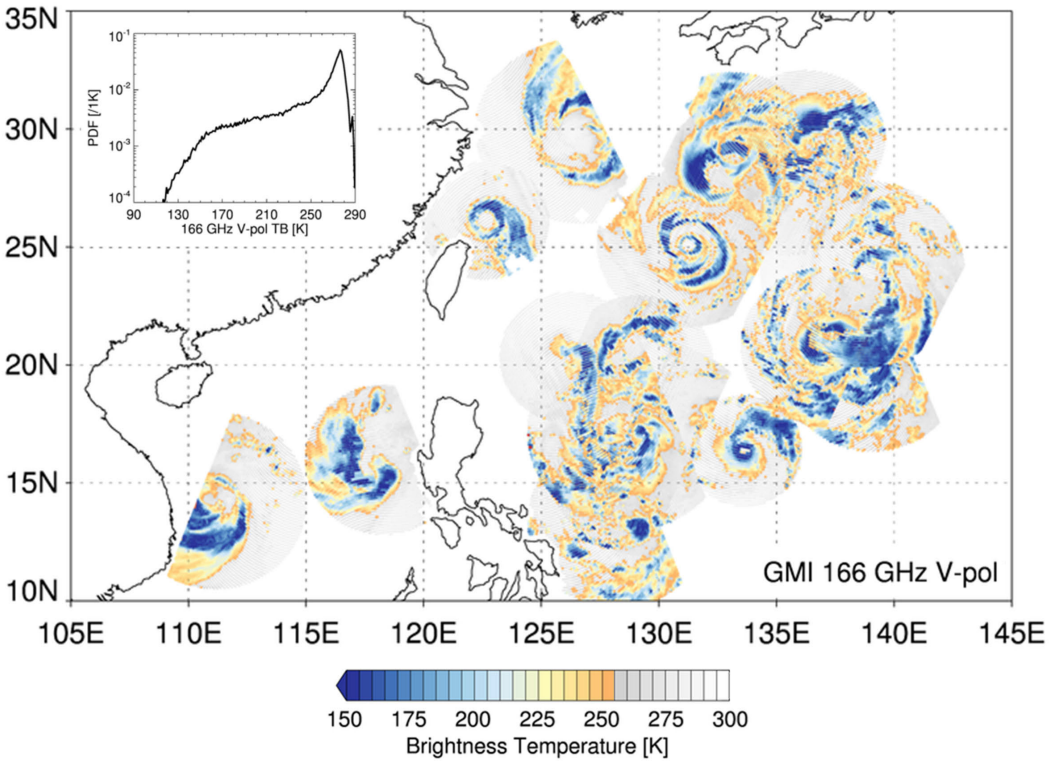

Fig. 8. GMI-observed TB at the 166-GHz V-pol channel for the tropical cyclones considered in the study. Land and ocean surfaces are distinguished using the MODIS MCD12C1 version 6 land/ocean mask, and data above land surfaces are excluded. Only data located within the ROCI of the tropical cyclones are used. Their pdf plot is shown in the top left corner.

indicating that higher frequency channels are more efficiently scattered by small particles. Thus, the 183.31-GHz channels have the greatest scattering efficiency. In addition, these channels have low transmittance (i.e., high optical thickness) for water vapor, resulting in weighting function peaks at altitudes higher than the ground level. As the frequency approaches 183.31 GHz, the altitude at which the weighting function peaks tends to increase. This peak altitude tends to be higher in warmer and wetter conditions than in colder and drier conditions, as shown in [86]. As the peak altitude increases, the scattering reduction in these channels becomes increasingly likely due to the smaller ice particles.

Fig. 9(a)–(j) demonstrates simulated TBs derived from different ice habits, along with Fig. 9(k) showing GMI observation at the 166-GHz V-pol channel for the tropical cyclone "HAISHEN" at 09:20 UTC on September 3, 2020. This specific example is chosen from the targeted cases. As anticipated, the WRF simulations exhibit discrepancies in terms of the location, shape, and intensity of the tropical cyclone compared to the observations. The current NWP models cannot accurately predict hydrometeors on a small scale. Nevertheless, if the microphysical properties are realistically represented, the simulated TB distribution will closely resemble the observed distribution. Fig. 9 shows that in areas where ice particles exist, *Soft Sphere* [see Fig. 9(b)], *Evans Snow Aggregate*[see Fig. 9(c)], and *Large Column Aggregate* [see Fig. 9(e)] generally result in weaker scattering signals than observations [see Fig. 9(k)]. Conversely, *8-Column Aggregate* [see Fig. 9(d)] and *Spherical Graupel* [see Fig. 9(h)] lead to strong scattering signals below 150 K over large areas. Moreover, the scattering signals simulated by *Large Block Aggregate* [see Fig. 9(g)] are weaker than those simulated by the former two but still stronger than the observed signals. The remaining ice habits, i.e., optimal ice habit [see Fig. 9(a)], *Large Plate Aggregate* [see Fig. 9(f)], *ICON Snow* [see Fig. 9(i)], and *GEM Snow* [see Fig. 9(j)], exhibit a relatively similar degree of scattering signal as the observations. However, the differences between them are difficult to visually distinguish in the figure.

The probability density functions (pdfs) of the RTM-simulated TBs (colored lines) are analyzed and compared with the GMI-observed TBs (black line), as shown in Fig. 10. This analysis is performed using the dataset of 19 tropical cyclones listed in Table III. Under clear-sky conditions, where the TB values are approximately 240 K or higher, no significant differences are observed in terms of the TB distribution between the simulations and observations. However, when the TBs decrease to below 240 K due to ice particle scattering, the simulated TB distributions exhibit substantial disparities. This pattern is observed for all the channels.

At the 89-GHz channel [see Fig. 10(a)], the simulations consistently display lower TB populations than the observations within the 200 K–250 K range. In comparison, this underestimation is less evident at the 183.31-GHz channels [see Fig. 10(c) and (d)], which predominantly responds to small ice particles suspended at higher altitudes. This underestimation could be due to the limitations inherent to the P3 microphysics scheme, which treats all ice species as a single category. Thus,

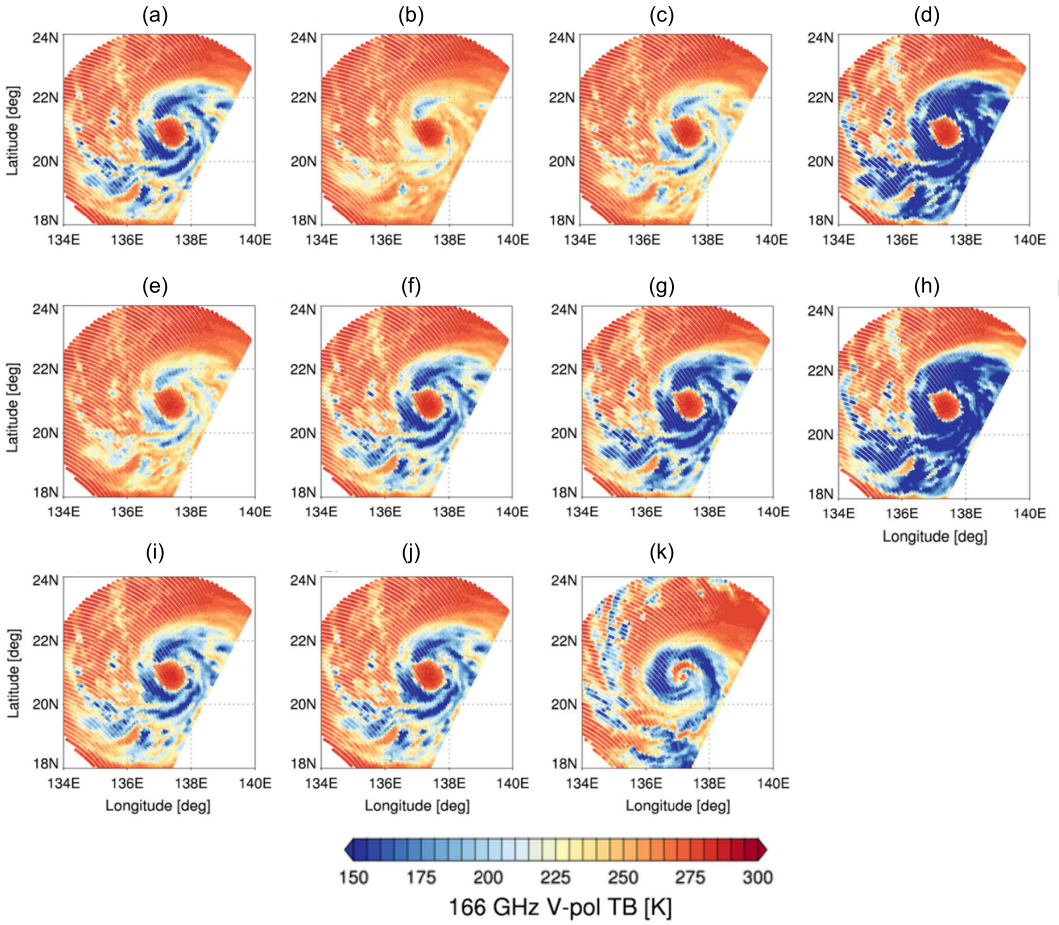

Fig. 9. RTM-simulated TBs: (a) optimal ice habits, (b)–(j) individual ice habits when used exclusively, and (k) the GMI-observed TB at 166 GHz V-pol channel. The targeted case is the tropical cyclone "HAISHEN" (09:20 UTC on September 3, 2020). (b) Soft Sphere. (c) Evans Snow Agg. (d) 8-Column Agg. (e) Large Column Agg. (f) Large Plate Agg. (g) Large Block Agg. (h) Spherical Graupel. (i) ICON Snow. (j) GEM Snow. (k) OBS.

this approach may not accurately simulate the number concentration of ice particles in regions where bimodal or multimodal PSDs are expected, resulting in lower concentrations of both small crystals and larger particles grown through aggregation or riming. This limitation is generally referred to as the "dilution problem" by Milbrandt and Morrison [87]. Furthermore, the secondary ice production considerably amplifies the number concentration of small nonspherical ice particles in mixed-phase clouds, specifically between 0 °C and −15 °C, as reported by Field et al. [75] and Zhao and Liu [88]. However, for the P3 scheme, with its single-category approach, the accurate simulation of their number concentrations is challenging, according to Qu et al. [89]. Moreover, water-coated ice particles within the melting layer can notably alter the scattering properties of microwaves (refer to [90]), but these particles are not accounted for in both the current RTM and the P3 scheme.

Despite these limitations, the results obtained using the optimal ice habit (red line) relatively well match the GMI observations. This agreement implies that accurate TB simulations can be realized by employing flexible microphysical properties and considering the inhomogeneity effect of ice habit distribution in microwave scattering simulations. In contrast, attempts to represent all ice particles with a single habit generally yield unsatisfactory results. Particularly, *8-Column Aggregate*, *Large Block Aggregate*, and *Spherical Graupel*, known as effective scatterers, tend to overestimate the scattering intensity across all scattering channels. As another effective scatterer, *GEM Snow* overestimates the scattering intensity at the 89-GHz channel, but its strong forward scattering (see Fig. 7) increases the amount of radiation reaching the top-of-atmosphere, resulting in a weaker overestimation compared to the three aforementioned habits. Conversely, *Soft Sphere*, *Evans Snow Aggregate*, and *Large Column Aggregate* tend to underestimate the scattering intensity across all scattering channels due to their lower scattering efficiencies. Moreover, strong forward scattering of *Soft Sphere* leads to the amplification of the overall underestimation, highlighting the limitations of assuming spherical shapes for ice particles in the RTM. Thus, realistic TB distributions cannot be obtained when representing all ice particles using these habits. Across all scattering channels, only *ICON Snow* and *Large Plate Aggregate* yield results comparable to the observations, along with the optimal ice habit, visually overlapping in Fig. 10.

C. Measures of Fit

Several fit measures are used to quantiitatively evaluate the performance of the RTM simulations. While widely utilized metrics such as the standard deviation, RMSE, and correlation coefficient are useful for quantifying the fit, they may be

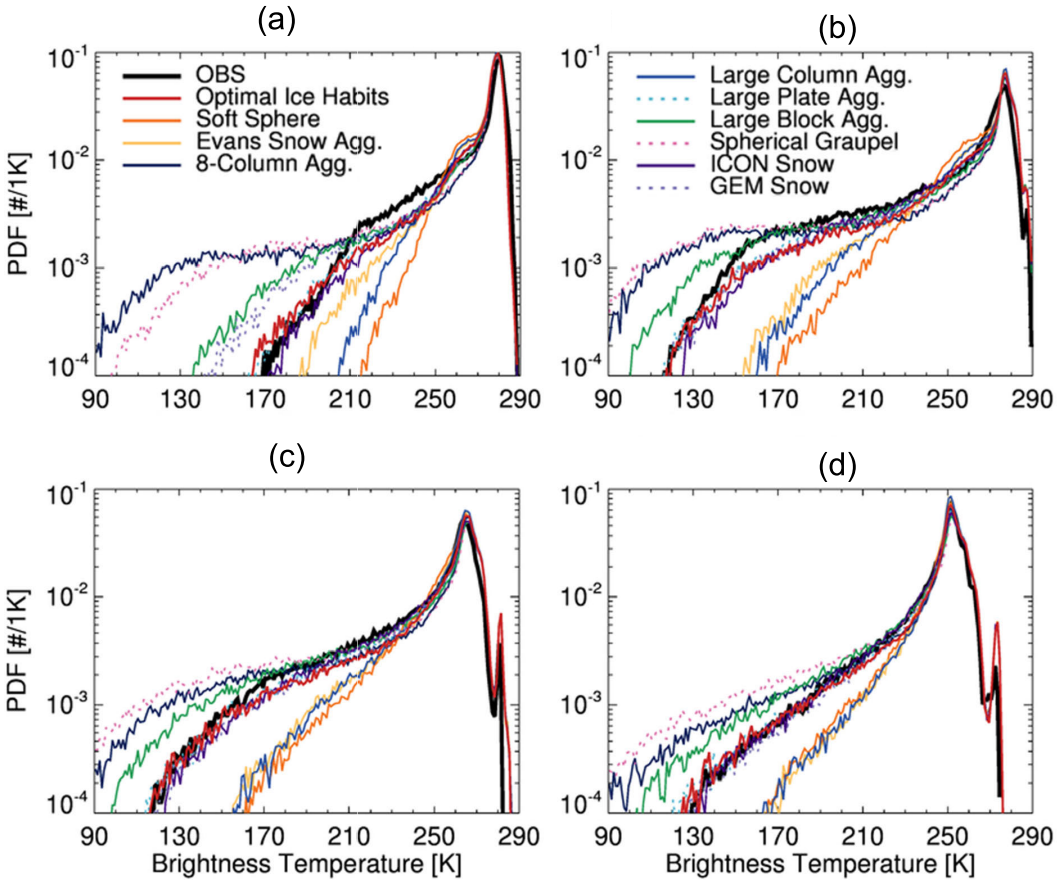

Fig. 10. PDFs of TBs at (a) 89-GHz V-pol, (b) 166-GHz V-pol, (c) 183 ± 7 GHz, and (d) 183 ± 3 GHz for the tropical cyclones listed in Table III. The different colored lines represent different ice habits (see legend), while the black line indicates GMI observations.

influenced by location errors stemming from the NWP model itself, which is commonly known as the "double penalty" issue. Furthermore, measures that are sensitive to relatively rare events, such as cloudy pixels, need to be considered to evaluate the scattering effect caused by ice particles.

An alternative measure is comparing the mean TBs between the observations and simulations, focusing on determining errors occurring during ice scattering. To isolate these cases, clear-sky pixels are filtered out by considering TBs below the threshold of 240 K for each channel, as proposed by Ekelund et al. [62]. The mean TBs are calculated as follows:

$$\overline{\mathrm{TB}} = \frac{\int_0^{240} \mathrm{TB} N(\mathrm{TB}) d\mathrm{TB}}{\int_0^{240} N(\mathrm{TB}) d\mathrm{TB}} \tag{15}$$

where $N(\mathrm{TB})$ represents the TB distribution and $d\mathrm{TB}$ is set as 1.0 K. Subsequently, the difference in mean TBs is calculated as

$$\Delta\overline{\mathrm{TB}}_{<240} = \overline{\mathrm{TB}}_{\mathrm{sim}} - \overline{\mathrm{TB}}_{\mathrm{obs}}. \tag{16}$$

The second alternative measure is the skewness of the histogram, which depicts the differences between the observed and simulated TBs. Although location errors may exist between the two datasets, the histogram tends to exhibit a symmetric bell curve with a skewness value close to zero when the TB distributions are similar. Skewness is sensitive to outliers (refer to [38] and [91]), eliminating the need to filter out clear-sky cases.

The final alternative measure is the TB histogram fit (h), which was introduced by Geer and Baordo [38]. This measure assesses the discrepancies between the histograms of the observations and simulations. It is a modification of the Kullback and Leibler [92] divergence, where the weighting term in each bin is removed. The modification enhances the sensitivity of measuring the histogram differences, particularly within bins with small population sizes. The measure is defined as follows:

$$h = \frac{1}{\#\mathrm{bins}_{\mathrm{obs}}} \sum_{\mathrm{bins}} \left| \log\left(\frac{\#\mathrm{sim}}{\#\mathrm{obs}}\right) \right| \tag{17}$$

where #obs and #sim represent the TB populations in each bin for the observations and simulations, respectively, and the bin size is set as 1.0 K. To prevent the infinity problem caused by bins with zero populations, a value of 0.1 is assigned to such bins. The TB histogram fit penalizes both excessive and insufficient scattering, as described in [38].

Fig. 11 presents the fit measures for all the scattering channels. Measures close to zero indicate good performance. In the figure, the top figure displays the mean differences between the RTM-simulated and GMI-observed TBs below 240 K. Similar to the pdf analysis, *8-Column Aggregate*, *Large Block Aggregate*, and *Spherical Graupel* consistently overestimate

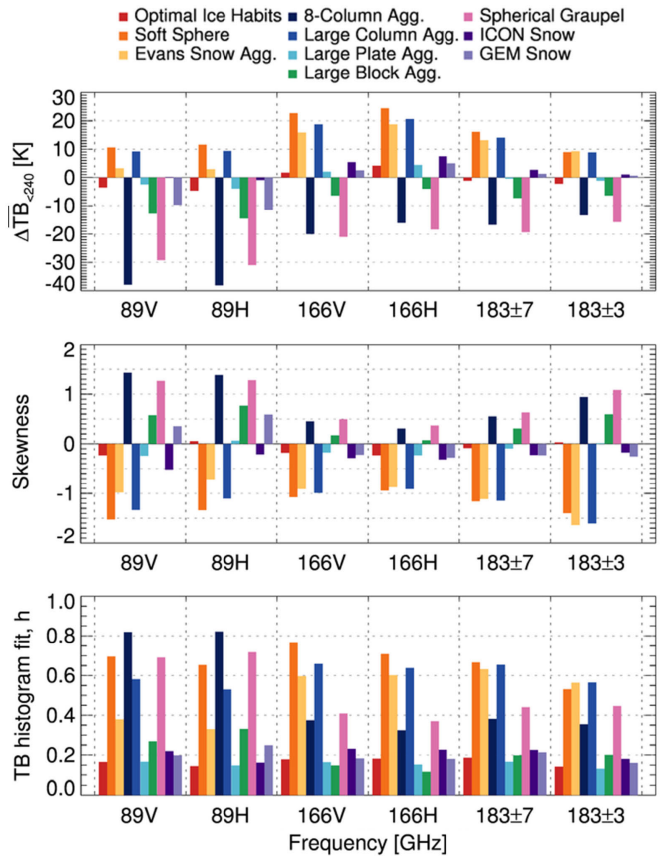

Fig. 11. Measures of fit between the RTM-simulated and GMI-observed TBs for all scattering channels. (Top) Mean differences below 240 K ($\Delta\overline{\mathrm{TB}}_{<240}$). (Middle) Skewness. (Bottom) TB histogram fit (h).

the scattering (negative $\Delta\overline{\mathrm{TB}}_{<240}$) across all scattering channels. Particularly, *8-Column Aggregate* and *Spherical Graupel* have considerable $\Delta\overline{\mathrm{TB}}_{<240}$ values of approximately -30 to -40 K at the 89-GHz channels. Conversely, *Soft Sphere*, *Evans Snow Aggregate*, and *Large Column Aggregate* tend to underestimate the scattering, resulting in positive $\Delta\overline{\mathrm{TB}}_{<240}$ values of approximately 10 K–25 K across all scattering channels, with the exception of *Evans Snow Aggregate* at the 89-GHz channels. Among the different habits considered, only the optimal ice habit, *Large Plate Aggregate*, and *ICON Snow* have $\Delta\overline{\mathrm{TB}}_{<240}$ values below the absolute value of 10 K across all scattering channels.

The middle figure of Fig. 11 illustrates the skewness of the TB difference histogram. A positive skewness value indicates a longer tail on the right side of the histogram, suggesting an underestimation of the simulated TBs and consequently implying excessive scattering. Conversely, a negative skewness value suggests insufficient scattering. A notable feature is the consistent negative skewness exhibited by *ICON Snow*, ranging from -0.2 to -0.5. These values are relatively worse than those of the optimal ice habit and *Large Plate Aggregate*.

The bottom figure of Fig. 11 presents the TB histogram fit results. Among all the ice habits, only the optimal ice habit and *Large Plate Aggregate* have h values of less than 0.2 across all scattering channels, indicating a good fit between the simulated and observed TBs. In addition, *ICON Snow* consistently demonstrates worse h values than the above two habits. In contrast, *8-Column Aggregate*, *Large Column Aggregate*, *Spherical Graupel*, *Soft Sphere*, and *Evans Snow Aggregate* do not have h values below 0.3 in any scattering channel, suggesting a poor fit between the simulated and observed TBs.

Table IV presents a comprehensive comparison of the measures across all scattering channels, where rms is used for $\Delta\overline{\mathrm{TB}}_{<240}$ and skewness and mean are employed for the histogram fit. Notably, the optimal ice habit and *Large Plate Aggregate* consistently yield the most favorable values for the three measures. The strength of the optimal ice habit lies in its ability to effectively capture the spatiotemporal variability of ice habits, which is not a feature found in other ice habits, including *Large Plate Aggregate*. This inherent capability stems from the physical mechanisms governing crystal formation and growth, as discussed in Section III-C, which enables the simulations to realistically represent a wide range of ice-scattering situations rather than just specific scenarios.

In this study, the performance difference between the optimal ice habit and *Large Plate Aggregate* is insignificant, mainly due to the limited focus on developed tropical cyclones over the ocean. As shown in Fig. 6(c), the optimal ice habit of developed tropical cyclones predominantly comprises *Large Plate Aggregate*, particularly in areas where ice particles grow through aggregation. Furthermore, in window channels with frequencies below 200 GHz, scattering within these areas significantly influences the resulting TB values. Hence, using only *Large Plate Aggregate* to represent the entire cloud

TABLE IV

COMPARISON OF FIT MEASURES BETWEEN RTM-SIMULATED AND GMI-OBSERVED TBS. TO PROVIDE A COMPREHENSIVE OVERVIEW OF THE STATISTIC SCORES, AN AVERAGE VALUE IS CALCULATED ACROSS ALL SCATTERING CHANNELS. FOR THE $\Delta\overline{TB}_{<240}$ AND SKEWNESS, THE RMS VALUE IS USED INSTEAD OF THE MEAN

Ice habits	$\Delta\overline{TB}_{<240}$ [K]	Skewness	TB histogram fit
Optimal ice habit	3.178	0.157	0.166
Soft Sphere	16.793	1.253	0.670
Evans Snow Aggregate	12.085	1.077	0.517
8-Column Aggregate	25.786	0.953	0.512
Large Column Aggregate	14.259	1.202	0.604
Large Plate Aggregate	2.771	0.160	0.154
Large Block Aggregate	9.345	0.483	0.210
Spherical Graupel	23.113	0.930	0.512
ICON Snow	3.944	0.308	0.207
GEM Snow	6.533	0.346	0.197

may be a reasonable and efficient option for this specific precipitation system and within this frequency range. However, it is unrealistic and unsuitable for all kinds of cloud conditions. Notably, the regions with the most significant differences in simulated TBs between the optimal ice habit and *Large Plate Aggregate* were the edges of the cyclones (as detailed in the Appendix), where *Large Plate Aggregate* demonstrated a stronger scattering intensity. This finding suggests that there is a considerable difference between the two approaches, particularly in terms of the horizontal inhomogeneity of ice habits. Meanwhile, Ekelund et al. [62] showed that for a mesoscale convective system, which includes a deep convection core and some cirrus, *Large Column Aggregate* and *Evans Snow Aggregate* are the best-matched habits at GMI channels exceeding 166 GHz. In addition, for frequencies above 200 GHz, scattering signals are mainly influenced by smaller ice particles in the upper troposphere as these smaller ice particles saturate the scattering and water vapor absorption occurs at higher altitudes, as described in [93]. In such cases, using only *Large Plate Aggregate* can lead to errors in the TB simulations, resulting in inaccurate outcomes.

D. Extending Frequency to 664 GHz

No measurements are currently available at frequencies above 200 GHz for validation. However, promising progress in this regard has been made with the upcoming launch of the Ice Cloud Imager (ICI) instrument aboard the Meteorological Operational Second Generation (MetOp-SG) satellite B. The anticipated launch of the ICI instrument in 2025 will expand the frequency coverage from 183 to 664 GHz, significantly enhancing the capability to detect small ice particles within anvil clouds, as described in [94] and [95].

This study further conducts TB simulations using the specifications of the ICI sensor's 664 ± 4.2-GHz V-pol channel. However, the FASTEM-6 model provides realistic estimates of the sea-surface emissivity only up to 200 GHz. To overcome this limitation, this study utilizes the Tool to Estimate the Sea-Surface Emissivity at Microwaves (TESSEM) model, which is known for its capability of providing reasonable emissivity values across a broad range of frequencies (refer to [96]).

Fig. 12 presents the TB distributions obtained with *Soft Sphere*, *Evans Snow Aggregate*, *Large Plate Aggregate*, and the optimal ice habit corresponding to the P3 microphysics, using the dataset from the 19 tropical cyclones detailed in Table III. Below 200 GHz, the TB distribution of *Large Plate Aggregate* closely resembles that of the optimal ice habit, while *Evans Snow Aggregate* and *Soft Sphere* exhibit relatively weaker scattering signals than the optimal ice habit (see Figs. 9–11). However, at 664 ± 4.2 GHz, the TB distributions simulated with the optimal ice habit are relatively similar to those of *Evans Snow Aggregate* and *Soft Sphere* rather than those of *Large Plate Aggregate*, as shown in Fig. 12. This difference is related to the significant change in the microphysical properties of ice crystals according to the vertical cloud structure. According to past observational studies, including [97], [98], and [99], large ice particles predominantly exist as aggregates in the lower sections of deep convective systems. Conversely, higher sections of deep convective systems are dominated by smaller ice crystals arising from vapor deposition. Therefore, *Large Plate Aggregate*, representative of ice particles grown through aggregation, may not suitably represent the smaller ice crystals found at higher altitudes.

Although no verifiable observations are currently available, this result highlights the distinction between representing all ice particles using *Large Plate Aggregate* and employing the optimal ice habit. Future studies and advancements in

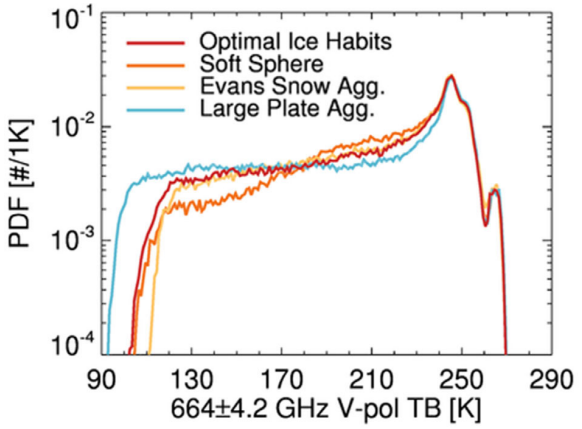

Fig. 12. PDFs of simulated TBs at 664 ± 4.2-GHz V-pol obtained using different ice particle habits: *Soft Sphere*, *Evans Snow Aggregate*, *Large Plate Aggregate*, and the optimal ice habit corresponding to the P3 microphysics. All the tropical cyclones listed in Table III are analyzed.

observational capabilities will provide further opportunities for improvements and validation. These study results will serve as valuable information for enhancing the accuracy and realism of RTM simulations, contributing to a better understanding of ice-scattering behaviors across a wide frequency spectrum.

V. Conclusion

This study improved the ice particle representation for passive microwave radiative transfer simulations. It exceeds the conventional "one-shape-fits-all" approach and adopts a more complex and realistic representation of ice clouds. This novel representation comprises a combination of diverse ice habits based on their microphysical properties, which was enabled by the flexibility of the P3 microphysics scheme.

The RMSE values of effective densities between four types of P3 ice crystals (including small, unrimed, completely rimed, and partially rimed crystals) and various ARTS ice habits (see Table I) were compared, with the aim of selecting the optimal combinations of ice habits that minimize the difference in the effective density. Importantly, the selection of the optimal habit depends on the crystal formation and growth mechanisms. In other words, the optimal habit proposed in this study can more effectively describe the spatiotemporal variability of ice habits than earlier approaches. Furthermore, the P3 scheme's inherent flexibility was instrumental in yielding a realistic representation of the ice habit distributions.

Moreover, an in-depth analysis of the scattering effects of the optimal ice habit was conducted by comparing the simulated and observed TBs at various scattering channels (e.g., 89, 166, 183.31±7, and 183.31±3 GHz). The tropical cyclone events observed by the GMI sensor in the Northwestern Pacific Ocean in 2020 were analyzed. Only cases meeting specific simulation error criteria (i.e., track error $\leq$ 120 km and MLSP error $\leq$ 20 hPa) were considered to ensure a reliable analysis. The simulated TBs were evaluated against the GMI-observed TBs.

The results demonstrate that the optimal ice habit proposed in this study consistently exhibits high performance across all fit measures, such as $\Delta\overline{\mathrm{TB}}_{<240}$, skewness, and TB histogram fit, signifying a substantial improvement in the scattering calculations. In the comprehensive evaluation across all scattering channels (refer to Table IV), no ice habits, with the exception of *Large Plate Aggregate*, outperformed the performance of the optimal ice habit when used exclusively. Especially, the assumption of representing all ice particles as spherical particles resulted in the considerable underestimation of their scattering intensity due to their unsuitable scattering properties (e.g., excessive forward scattering), as shown in previous studies, such as [27], [28], [29], [30], and [31]. This was pronounced at frequencies above 100 GHz, making it one of the most inappropriate ice habits. The study results emphasize the critical importance of realistically considering the representation of ice habits in microwave scattering calculations.

In addition, the analyses were extended to frequencies above 200 GHz, the observations for which are currently unavailable for validation but will be accessible with the upcoming launch of the ICI instrument aboard the MetOp-SG satellite. Preliminary simulations using the ICI sensor specifications at 664 ± 4.2-GHz V-pol channel afforded intriguing differences in the TB distributions of various ice habits, notably between the optimal ice habit and *Large Plate Aggregate*. These results highlight the growing necessity to consider the spatiotemporal variability of ice habits in microwave radiative transfer simulations with the expansion of the observational frequency spectrum.

Despite these advances, this study has certain limitations. First, the proposed representation of ice clouds is intrinsically dependent on the P3 microphysics scheme, which may constrain its applicability to other microphysics parameterizations. Second, and crucially, the current range of available ice habits in the ARTS scattering database is limited. This is particularly noticeable in representing dense and strongly rimed particles, as shown in Fig. 4. These particles do not agree well with the *Spherical Graupel* habit, indicating a difference in expressing the effective densities from the P3 scheme. It is necessary to strengthen the database to include a wider variety of ice particle habits, particularly those of rimed particles. Another critical concern is the lack of observational data that can quantify the changes in the ice crystal microphysical properties, such as size and shape distribution, in response to diverse environmental conditions. To overcome these limitations, interdisciplinary collaborations in these fields are highly important. Such joint research efforts will enable a more physically based representation of ice clouds, further improving the accuracy of RTMs.

In conclusion, this study takes a significant step forward in enhancing the realism and accuracy of passive microwave RTMs. It highlights the need for the continuous refinement of RTMs in coordination with advancements in observational capabilities and modeling techniques. The study results will help improve the understanding and forecasting of weather, climate, and water cycle patterns.

Appendix

In this Appendix, we present a further analysis of TB differences and microphysical details of the tropical cyclone

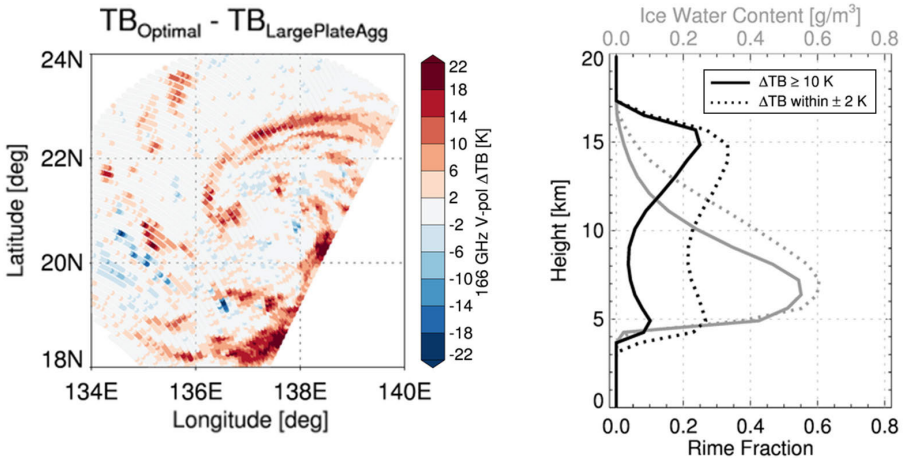

Fig. 13. Comparison of simulated TBs of the 166-GHz V-pol channel and corresponding microphysical properties for tropical cyclone "HAISHEN" captured at 09:20 UTC on September 3, 2020. (Left) TB difference between the optimal ice habit and *Large Plate Aggregate*. (Right) Averaging profiles of rime fraction (black lines) and IWC (gray lines) for ΔTB $\geq$ 10K (solid lines) versus ΔTB within $\pm$2K (dotted lines), conducted only where the IWP is over 0.5kg/m^2.

"HAISHEN" depicted in Fig. 9. The left figure of Fig. 13 illustrates the simulated TB differences between the optimal ice habit and *Large Plate Aggregate*. Our findings indicate that TB differences (ΔTB) are generally within -2 K to 2 K in most areas. However, significant differences are noted at the edges of the cyclone's rain bands: the optimal ice habit shows higher TBs, suggesting less scattering, compared to *Large Plate Aggregate*. The right figure of Fig. 13 displays the profiles of rime fraction in areas with high ΔTB ($\geq$ 10K) and those with minimal differences ($\pm$2K). The results show that areas with ΔTB above 10 K have much lower rime fractions, often below 0.1, indicating that *Large Plate Aggregate* has a stronger scattering intensity, especially where there is little riming at the cyclone's edges.

REFERENCES

[1] S. A. Klein et al., "Intercomparison of model simulations of mixed-phase clouds observed during the ARM mixed-phase Arctic cloud experiment. I: Single-layer cloud," *Quart. J. Roy. Meteorol. Soc.*, vol. 135, no. 641, pp. 979–1002, 2009.

[2] R. Forbes, A. J. Geer, K. Lonitz, and M. Ahlgrimm, "Reducing systematic errors in cold-air outbreaks," *ECMWF Newslett.*, vol. 146, pp. 17–22, Jan. 2016.

[3] A. J. Geer, "Physical characteristics of frozen hydrometeors inferred with parameter estimation," *Atmos. Meas. Techn.*, vol. 14, no. 8, pp. 5369–5395, Aug. 2021.

[4] C. Prigent, "Precipitation retrieval from space: An overview," *Comp. Rendus Geosci.*, vol. 342, nos. 4–5, pp. 380–389, Apr. 2010.

[5] A. J. Geer et al., "The growing impact of satellite observations sensitive to humidity, cloud and precipitation," *Quart. J. Roy. Meteorolog. Soc.*, vol. 143, no. 709, pp. 3189–3206, Oct. 2017.

[6] A. J. Geer et al., "All-sky satellite data assimilation at operational weather forecasting centres," *Quart. J. Roy. Meteorolog. Soc.*, vol. 144, no. 713, pp. 1191–1217, Apr. 2018.

[7] A. J. Geer et al., "Bulk hydrometeor optical properties for microwave and sub-millimetre radiative transfer in RTTOV-SCATT v13.0," *Geosci. Model Develop.*, vol. 14, no. 12, pp. 7497–7526, Dec. 2021.

[8] T. T. Wilheit, A. T. C. Chang, M. S. V. Rao, E. B. Rodgers, and J. S. Theon, "A satellite technique for quantitatively mapping rainfall rates over the oceans," *J. Appl. Meteorol.*, vol. 16, no. 5, pp. 551–560, May 1977.

[9] J. A. Weinman and R. Davies, "Thermal microwave radiances from horizontally finite clouds of hydrometeors," *J. Geophys. Res., Oceans*, vol. 83, no. C6, pp. 3099–3107, Jun. 1978.

[10] T. T. Wilheit et al., "Microwave radiometric observations near 19.35, 92 and 183 GHz of precipitation in tropical storm Cora," *J. Appl. Meteorol.*, vol. 21, no. 8, pp. 1137–1145, Aug. 1982.

[11] A. Mugnai and E. A. Smith, "Radiative transfer to space through a precipitating cloud at multiple microwave frequencies. Part I: Model description," *J. Appl. Meteorol.*, vol. 27, no. 9, pp. 1055–1073, Sep. 1988.

[12] R. F. Adler, H.-Y.-M. Yeh, N. Prasad, W.-K. Tao, and J. Simpson, "Microwave simulations of a tropical rainfall system with a three-dimensional cloud model," *J. Appl. Meteorol.*, vol. 30, no. 7, pp. 924–953, Jul. 1991.

[13] E. A. Smith, H. J. Cooper, X. Xiang, A. Mugnai, and G. J. Tripoli, "Foundations for statistical-physical precipitation retrieval from passive microwave satellite measurements. Part I: Brightness-temperature properties of a time-dependent cloud-radiation model," *J. Appl. Meteorol.*, vol. 31, no. 6, pp. 506–531, Jun. 1992.

[14] G. M. Skofronick-Jackson, A. J. Gasiewski, and J. R. Wang, "Influence of microphysical cloud parameterizations on microwave brightness temperatures," *IEEE Trans. Geosci. Remote Sens.*, vol. 40, no. 1, pp. 187–196, Feb. 2002.

[15] A. M. Doherty, T. R. Sreerekha, U. M. O'Keeffe, and S. J. English, "Ice hydrometeor microphysical assumptions in radiative transfer models at AMSU-B frequencies," *Quart. J. Roy. Meteorolog. Soc.*, vol. 133, no. 626, pp. 1205–1212, Jul. 2007.

[16] T. Matsui, X. Zeng, W.-K. Tao, H. Masunaga, W. S. Olson, and S. Lang, "Evaluation of long-term cloud-resolving model simulations using satellite radiance observations and multifrequency satellite simulators," *J. Atmos. Ocean. Technol.*, vol. 26, no. 7, pp. 1261–1274, Jul. 2009.

[17] T. Matsui et al., "Introducing multisensor satellite radiance-based evaluation for regional Earth system modeling," *J. Geophys. Res., Atmos.*, vol. 119, no. 13, pp. 8450–8475, Jul. 2014.

[18] J. J. Shi et al., "WRF simulations of the 20–22 January 2007 snow events over eastern Canada: Comparison with in situ and satellite observations," *J. Appl. Meteorol. Climatol.*, vol. 49, no. 11, pp. 2246–2266, Nov. 2010.

[19] M. Han, S. A. Braun, T. Matsui, and C. R. Williams, "Evaluation of cloud microphysics schemes in simulations of a winter storm using radar and radiometer measurements," *J. Geophys. Res., Atmos.*, vol. 118, no. 3, pp. 1401–1419, Feb. 2013.

[20] M. Han, S. A. Braun, T. Matsui, and T. Iguchi, "Comparisons of bin and bulk microphysics schemes in simulations of topographic winter precipitation with radar and radiometer measurements," *Quart. J. Roy. Meteorolog. Soc.*, vol. 144, no. 715, pp. 1926–1946, Jul. 2018.

[21] A. V. Korolev, G. A. Isaac, and J. Hallett, "Ice particle habits in Arctic clouds," *Geophys. Res. Lett.*, vol. 26, no. 9, pp. 1299–1302, May 1999.

[22] A. J. Heymsfield, "Properties of tropical and midlatitude ice cloud particle ensembles. Part I: Median mass diameters and terminal velocities," *J. Atmos. Sci.*, vol. 60, no. 21, pp. 2573–2591, Nov. 2003.

[23] C. D. Westbrook, R. C. Ball, P. R. Field, and A. J. Heymsfield, "Theory of growth by differential sedimentation, with application to snowflake formation," *Phys. Rev. E, Stat. Phys. Plasmas Fluids Relat. Interdiscip. Top.*, vol. 70, no. 2, Aug. 2004, Art. no. 021403.

[24] R. P. Lawson et al., "A review of ice particle shapes in cirrus formed in situ and in anvils," *J. Geophys. Res., Atmos.*, vol. 124, nos. 17–18, pp. 10049–10090, Sep. 2019.

[25] P. Bauer, "Including a melting layer in microwave radiative transfer simulation for clouds," *Atmos. Res.*, vol. 57, no. 1, pp. 9–30, Feb. 2001.

[26] S. B. Sieron, E. E. Clothiaux, F. Zhang, Y. Lu, and J. A. Otkin, "Comparison of using distribution-specific versus effective radius methods for hydrometeor single-scattering properties for all-sky microwave satellite radiance simulations with different microphysics parameterization schemes," *J. Geophys. Res., Atmos.*, vol. 122, no. 13, pp. 7027–7046, Jul. 2017.

[27] M. S. Kulie, R. Bennartz, T. J. Greenwald, Y. Chen, and F. Weng, "Uncertainties in microwave properties of frozen precipitation: Implications for remote sensing and data assimilation," *J. Atmos. Sci.*, vol. 67, no. 11, pp. 3471–3487, Nov. 2010.

[28] H. Nowell, G. Liu, and R. Honeyager, "Modeling the microwave single-scattering properties of aggregate snowflakes," *J. Geophys. Res., Atmos.*, vol. 118, no. 14, pp. 7873–7885, Jul. 2013.

[29] K.-S. Kuo et al., "The microwave radiative properties of falling snow derived from nonspherical ice particle models. Part I: An extensive database of simulated pristine crystals and aggregate particles, and their scattering properties," *J. Appl. Meteorol. Climatol.*, vol. 55, no. 3, pp. 691–708, Mar. 2016.

[30] W. S. Olson et al., "The microwave radiative properties of falling snow derived from nonspherical ice particle models. Part II: Initial testing using radar, radiometer and in situ observations," *J. Appl. Meteorol. Climatol.*, vol. 55, no. 3, pp. 709–722, Mar. 2016.

[31] S. Ringerud, M. S. Kulie, D. L. Randel, G. M. Skofronick-Jackson, and C. D. Kummerow, "Effects of ice particle representation on passive microwave precipitation retrieval in a Bayesian scheme," *IEEE Trans. Geosci. Remote Sens.*, vol. 57, no. 6, pp. 3619–3632, Jun. 2019.

[32] E. Purcell and C. Pennypacker, "DDA basics," *Astrophys. J.*, vol. 186, pp. 705–714, 1973.

[33] B. T. Draine and P. J. Flatau, "Discrete-dipole approximation for scattering calculations," *J. Opt. Soc. Amer. A, Opt. Image Sci.*, vol. 11, no. 4, p. 1491, 1994.

[34] R. Saunders et al., "An update on the RTTOV fast radiative transfer model (currently at version 12)," *Geosci. Model Develop.*, vol. 11, no. 7, pp. 2717–2737, Jul. 2018.

[35] F. Weng, "Advances in radiative transfer modeling in support of satellite data assimilation," *J. Atmos. Sci.*, vol. 64, no. 11, pp. 3799–3807, Nov. 2007.

[36] B. Johnson, T. Zhu, M. Chen, Y. Ma, and T. Auligne, "The community radiative transfer model (CRTM)," in *Proc. 21st Int. TOVS Study Conf.*, Darmstadt, Germany, 2017, pp. 1–24.

[37] S. B. Sieron, F. Zhang, E. E. Clothiaux, L. N. Zhang, and Y. Lu, "Representing precipitation ice species with both spherical and nonspherical particles for radiative transfer modeling of microphysics-consistent cloud microwave scattering properties," *J. Adv. Model. Earth Syst.*, vol. 10, no. 4, pp. 1011–1028, Apr. 2018.

[38] A. J. Geer and F. Baordo, "Improved scattering radiative transfer for frozen hydrometeors at microwave frequencies," *Atmos. Meas. Techn.*, vol. 7, no. 6, pp. 1839–1860, Jun. 2014.

[39] G. M. McFarquhar, A. J. Heymsfield, A. Macke, J. Iaquinta, and S. M. Aulenbach, "Use of observed ice crystal sizes and shapes to calculate mean-scattering properties and multispectral radiances: CEPEX April 4, 1993, case study," *J. Geophy. Res. Atmos.*, vol. 104, no. D24, pp. 31763–31779, 1999.

[40] P. Rolland, K. N. Liou, M. D. King, S. C. Tsay, and G. M. McFarquhar, "Remote sensing of optical and microphysical properties of cirrus clouds using moderate-resolution imaging spectroradiometer channels: Methodology and sensitivity to physical assumptions," *J. Geophys. Res., Atmos.*, vol. 105, no. D9, pp. 11721–11738, May 2000.

[41] G. M. McFarquhar, P. Yang, A. Macke, and A. J. Baran, "A new parameterization of single scattering solar radiative properties for tropical anvils using observed ice crystal size and shape distributions," *J. Atmos. Sci.*, vol. 59, no. 16, pp. 2458–2478, Aug. 2002.

[42] B. A. Baum et al., "Bulk scattering properties for the remote sensing of ice clouds. Part II: Narrowband models," *J. Appl. Meteorol.*, vol. 44, no. 12, pp. 1896–1911, Dec. 2005.

[43] A. J. Baran and L. Labonnote, "A self-consistent scattering model for cirrus. I: The solar region," *Quart. J. Roy. Meteorolog. Soc.*, vol. 133, no. 629, pp. 1899–1912, Oct. 2007.

[44] M. Barreyat, P. Chambon, J. Mahfouf, and G. Faure, "A 1D Bayesian inversion of microwave radiances using several radiative properties of solid hydrometeors," *Atmos. Sci. Lett.*, vol. 24, no. 3, p. e1142, Mar. 2023.

[45] H. Morrison and J. A. Milbrandt, "Parameterization of cloud microphysics based on the prediction of bulk ice particle properties. Part I: Scheme description and idealized tests," *J. Atmos. Sci.*, vol. 72, no. 1, pp. 287–311, Jan. 2015.

[46] M. Kazumori and S. J. English, "Use of the ocean surface wind direction signal in microwave radiance assimilation," *Quart. J. Roy. Meteorolog. Soc.*, vol. 141, no. 689, pp. 1354–1375, Apr. 2015.

[47] H. J. Liebe, G. A. Hufford, and M. Cotton, "Propagation modeling of moist air and suspended water/ice particles at frequencies below 1000 GHz," in *Proc. AGARD 52nd Spec. Meeting Electromagn. Wave Propag. Panel Symp.*, Palma de Mallorca, Spain, 1993, pp. 1–10.

[48] J. H. Joseph, W. J. Wiscombe, and J. A. Weinman, "The delta-Eddington approximation for radiative flux transfer," *J. Atmos. Sci.*, vol. 33, no. 12, pp. 2452–2459, Dec. 1976.

[49] C. Kummerow, "On the accuracy of the Eddington approximation for radiative transfer in the microwave frequencies," *J. Geophys. Res., Atmos.*, vol. 98, no. D2, pp. 2757–2765, Feb. 1993.

[50] A. J. Geer, P. Bauer, and C. W. O'Dell, "A revised cloud overlap scheme for fast microwave radiative transfer in rain and cloud," *J. Appl. Meteorol. Climatol.*, vol. 48, no. 11, pp. 2257–2270, Nov. 2009.

[51] C. Mätzler, "Microwave dielectric properties of ice," in *Thermal Microwave Radiation: Applications for Remote Sensing*, vol. 52. Stevenage, U.K.: IET, 2006, ch. 5, pp. 455–462.

[52] V. Barlakas, A. J. Geer, and P. Eriksson, "Introducing hydrometeor orientation into all-sky microwave and submillimeter assimilation," *Atmos. Meas. Techn.*, vol. 14, no. 5, pp. 3427–3447, May 2021.

[53] A. Y. Hou et al., "The global precipitation measurement mission," *Bull. Amer. Meteorol. Soc.*, vol. 95, pp. 701–722, May 2014.

[54] C. F. Bohren and D. R. Huffman, *Absorption and Scattering of Light by Small Particles*. Hoboken, NJ, USA: Wiley, 2008.

[55] J. M. Garnett, "VII. Colours in metal glasses, in metallic films, and in metallic solutions.—II," *Philos. Trans. Roy. Soc. A*, vol. 205, nos. 387–401, pp. 237–288, 1906.

[56] G. Tang, P. Yang, P. G. Stegmann, R. Lee Panetta, L. Tsang, and B. Johnson, "Effect of particle shape, density, and inhomogeneity on the microwave optical properties of graupel and hailstones," *IEEE Trans. Geosci. Remote Sens.*, vol. 55, no. 11, pp. 6366–6378, Nov. 2017.

[57] D. Ori and S. Kneifel, "Assessing the uncertainties of the discrete dipole approximation in case of melting ice particles," *J. Quant. Spectrosc. Radiat. Transf.*, vol. 217, pp. 396–406, Sep. 2018.

[58] G. Liu, "A database of microwave single-scattering properties for nonspherical ice particles," *Bull. Amer. Meteorolog. Soc.*, vol. 89, no. 10, pp. 1563–1570, Oct. 2008.

[59] G. Hong et al., "Scattering database in the millimeter and submillimeter wave range of 100–1000 GHz for nonspherical ice particles," *J. Geophys. Res., Atmos.*, vol. 114, no. D6, pp. 1–12, Mar. 2009.

[60] P. Eriksson, R. Ekelund, J. Mendrok, M. Brath, O. Lemke, and S. A. Buehler, "A general database of hydrometeor single scattering properties at microwave and sub-millimetre wavelengths," *Earth Syst. Sci. Data*, vol. 10, no. 3, pp. 1301–1326, Jul. 2018.

[61] M. Brath, R. Ekelund, P. Eriksson, O. Lemke, and S. A. Buehler, "Microwave and submillimeter wave scattering of oriented ice particles," *Atmos. Meas. Techn.*, vol. 13, no. 5, pp. 2309–2333, May 2020.

[62] R. Ekelund, P. Eriksson, and S. Pfreundschuh, "Using passive and active observations at microwave and sub-millimetre wavelengths to constrain ice particle models," *Atmos. Meas. Techn.*, vol. 13, no. 2, pp. 501–520, Feb. 2020.

[63] S. Pfreundschuh et al., "Synergistic radar and sub-millimeter radiometer retrievals of ice hydrometeors in mid-latitude frontal cloud systems," *Atmos. Meas. Techn.*, vol. 15, no. 3, pp. 677–699, Feb. 2022.

[64] C. G. Schmitt and A. J. Heymsfield, "Observational quantification of the separation of simple and complex atmospheric ice particles," *Geophys. Res. Lett.*, vol. 41, no. 4, pp. 1301–1307, Feb. 2014.

[65] E. J. Mlawer, S. J. Taubman, P. D. Brown, M. J. Iacono, and S. A. Clough, "Radiative transfer for inhomogeneous atmospheres: RRTM, a validated correlated-k model for the longwave," *J. Geophys. Res., Atmos.*, vol. 102, no. D14, pp. 16663–16682, Jul. 1997.

[66] J. S. Kain and J. M. Fritsch, "A one-dimensional entraining/detraining plume model and its application in convective parameterization," *J. Atmos. Sci.*, vol. 47, no. 23, pp. 2784–2802, Dec. 1990.

[67] S.-Y. Hong, Y. Noh, and J. Dudhia, "A new vertical diffusion package with an explicit treatment of entrainment processes," *Monthly Weather Rev.*, vol. 134, no. 9, pp. 2318–2341, Sep. 2006.

[68] P. R. A. Brown and P. N. Francis, "Improved measurements of the ice water content in cirrus using a total-water probe," *J. Atmos. Ocean. Technol.*, vol. 12, no. 2, pp. 410–414, Apr. 1995.
[69] R. J. Hogan, L. Tian, P. R. A. Brown, C. D. Westbrook, A. J. Heymsfield, and J. D. Eastment, "Radar scattering from ice aggregates using the horizontally aligned oblate spheroid approximation," *J. Appl. Meteorol. Climatol.*, vol. 51, no. 3, pp. 655–671, Mar. 2012.
[70] H. Morrison, J. A. Curry, and V. I. Khvorostyanov, "A new double-moment microphysics parameterization for application in cloud and climate models. Part I: Description," *J. Atmos. Sci.*, vol. 62, no. 6, pp. 1665–1677, Jun. 2005.
[71] K.-S.-S. Lim and S.-Y. Hong, "Development of an effective double-moment cloud microphysics scheme with prognostic cloud condensation nuclei (CCN) for weather and climate models," *Monthly Weather Rev.*, vol. 138, no. 5, pp. 1587–1612, May 2010.
[72] J. Kim, D.-B. Shin, and D. Kim, "Considering various multimoment bulk microphysics schemes for simulation of passive microwave radiative signatures," *IEEE Trans. Geosci. Remote Sens.*, vol. 60, pp. 1–15, 2022, Art. no. 4106115.
[73] K. G. Libbrecht, "Physical dynamics of ice crystal growth," *Annu. Rev. Mater. Res.*, vol. 47, no. 1, pp. 271–295, Jul. 2017.
[74] F. J. Tapiador, J.-L. Sánchez, and E. García-Ortega, "Empirical values and assumptions in the microphysics of numerical models," *Atmos. Res.*, vol. 215, pp. 214–238, Jan. 2019.
[75] P. R. Field et al., "Ice formation and evolution in clouds and precipitation: Measurement and modeling challenges: Chapter 7. Secondary ice production-current state of the science and recommendations for the future," *Meteorol. Monographs*, vol. 58, pp. 7.1–7.20, Jan. 2017.
[76] J. Yon, A. Bescond, and F.-X. Ouf, "A simple semi-empirical model for effective density measurements of fractal aggregates," *J. Aerosol Sci.*, vol. 87, pp. 28–37, Sep. 2015.
[77] L. Peng and Y. Liu, "Theoretical foundation of the relationship between three definitions of effective density and particle size," *Atmosphere*, vol. 13, no. 4, p. 564, Mar. 2022.
[78] H. Morrison, J. A. Milbrandt, G. H. Bryan, K. Ikeda, S. A. Tessendorf, and G. Thompson, "Parameterization of cloud microphysics based on the prediction of bulk ice particle properties. Part II: Case study comparisons with observations and other schemes," *J. Atmos. Sci.*, vol. 72, no. 1, pp. 312–339, Jan. 2015.
[79] J. Um and G. M. McFarquhar, "Single-scattering properties of aggregates of plates," *Quart. J. Roy. Meteorolog. Soc.*, vol. 135, no. 639, pp. 291–304, Jan. 2009.
[80] R. Ekelund, M. Brath, J. Mendrok, and P. Eriksson, "ARTS microwave single scattering properties database," Zenodo, CERN, Geneva, Switzerland, Tech. Rep., 2018.
[81] T. R. Knutson, J. J. Sirutis, S. T. Garner, I. M. Held, and R. E. Tuleya, "Simulation of the recent multidecadal increase of Atlantic hurricane activity using an 18-km-Grid regional model," *Bull. Amer. Meteorolog. Soc.*, vol. 88, no. 10, pp. 1549–1565, Oct. 2007.
[82] C. Davis et al., "Prediction of landfalling hurricanes with the advanced hurricane WRF model," *Monthly Weather Rev.*, vol. 136, no. 6, pp. 1990–2005, Jun. 2008.
[83] M. Xue, J. Schleif, F. Kong, K. W. Thomas, Y. Wang, and K. Zhu, "Track and intensity forecasting of hurricanes: Impact of convection-permitting resolution and global ensemble Kalman filter analysis on 2010 Atlantic season forecasts," *Weather Forecasting*, vol. 28, no. 6, pp. 1366–1384, Dec. 2013.
[84] K. T. F. Chan and J. C. L. Chan, "Sensitivity of the simulation of tropical cyclone size to microphysics schemes," *Adv. Atmos. Sci.*, vol. 33, no. 9, pp. 1024–1035, Sep. 2016.
[85] A. F. Prein, R. M. Rasmussen, D. Wang, and S. E. Giangrande, "Sensitivity of organized convective storms to model grid spacing in current and future climates," *Phil. Trans. Roy. Soc. A, Math., Phys. Eng. Sci.*, vol. 379, no. 2195, Apr. 2021, Art. no. 20190546.
[86] L. Edel, J.-F. Rysman, C. Claud, C. Palerme, and C. Genthon, "Potential of passive microwave around 183 GHz for snowfall detection in the Arctic," *Remote Sens.*, vol. 11, no. 19, p. 2200, Sep. 2019.
[87] J. A. Milbrandt and H. Morrison, "Parameterization of cloud microphysics based on the prediction of bulk ice particle properties. Part III: Introduction of multiple free categories," *J. Atmos. Sci.*, vol. 73, no. 3, pp. 975–995, Mar. 2016.
[88] X. Zhao and X. Liu, "Global importance of secondary ice production," *Geophys. Res. Lett.*, vol. 48, no. 11, Jun. 2021, Art. no. e2021GL092581.
[89] Z. Qu et al., "The impacts of secondary ice production on microphysics and dynamics in tropical convection," *Atmos. Chem. Phys.*, vol. 22, no. 18, pp. 12287–12310, Sep. 2022.
[90] V. S. Galligani, C. Prigent, E. Defer, C. Jimenez, and P. Eriksson, "The impact of the melting layer on the passive microwave cloud scattering signal observed from satellites: A study using TRMM microwave passive and active measurements," *J. Geophys. Res., Atmos.*, vol. 118, no. 11, pp. 5667–5678, Jun. 2013.
[91] D. S. Wilks, *Statistical Methods in the Atmospheric Sciences*, 3rd ed. New York, NY, USA: Academic, 2011, ch. 3, pp. 27–28.
[92] S. Kullback and R. A. Leibler, "On information and sufficiency," *Ann. Math. Statist.*, vol. 22, no. 1, pp. 79–86, 1951.
[93] S. Fox, "An evaluation of radiative transfer simulations of cloudy scenes from a numerical weather prediction model at sub-millimetre frequencies using airborne observations," *Remote Sens.*, vol. 12, no. 17, p. 2758, Aug. 2020.
[94] M. Bergadá et al., "The ice cloud imager (ICI) preliminary design and performance," in *Proc. 14th Specialist Meeting Microw. Radiometry Remote Sens. Environ. (MicroRad)*, Apr. 2016, pp. 27–31.
[95] P. Eriksson et al., "Towards an operational ice cloud imager (ICI) retrieval product," *Atmos. Meas. Techn.*, vol. 13, no. 1, pp. 53–71, Jan. 2020.
[96] C. Prigent, F. Aires, D. Wang, S. Fox, and C. Harlow, "Sea-surface emissivity parametrization from microwaves to millimetre waves," *Quart. J. Roy. Meteorolog. Soc.*, vol. 143, no. 702, pp. 596–605, Jan. 2017.
[97] P. Yang et al., "Single-scattering properties of droxtals," *J. Quant. Spectrosc. Radiat. Transf.*, vols. 79–80, pp. 1159–1169, Jun. 2003.
[98] J. Whiteway et al., "Anatomy of cirrus clouds: Results from the emerald airborne campaigns," *Geophys. Res. Lett.*, vol. 31, no. 24, pp. 1–10, Dec. 2004.
[99] M. W. Gallagher et al., "Observations and modelling of microphysical variability, aggregation and sedimentation in tropical anvil cirrus outflow regions," *Atmos. Chem. Phys.*, vol. 12, no. 14, pp. 6609–6628, Jul. 2012.

Jiseob Kim was born in Kangwon, South Korea, in 1991. He received the B.S. degree in atmospheric sciences and the Ph.D. degree from Yonsei University, Seoul, South Korea, in 2016 and 2023, respectively.

He is currently a Post-Doctoral Researcher with Yonsei University. His research interests include the interaction of microwaves with ice particles within microwave radiative transfer models and precipitation retrievals from observed microwave radiances based on a deep understanding of their microphysical processes.

Dong-Bin Shin received the B.S. and M.S. degrees in atmospheric sciences from Yonsei University, Seoul, South Korea, in 1987 and 1989, respectively, and the Ph.D. degree in atmospheric sciences from Texas A&M University, College Station, TX, USA, in 1999.

He was a Research Professor with the Center for Earth Observing and Space Research, School of Computational Sciences, George Mason University, Fairfax, VA, USA, and a Research Associate with the Department of Atmospheric Science, Colorado State University, Fort Collins, CO, USA, from 2000 to 2007. He is currently with the Department of Atmospheric Sciences, Yonsei University, where, first, he was an Associate Professor and, then, has been a Professor since 2007. His research interests include physically based remote sensing of clouds and precipitation from infrared and microwave observations and microwave radiative transfer modeling. His research also focuses on understanding global and regional hydrological balances.

Donghyeck Kim was born in Busan, South Korea, in 1993. He received the B.S. degree in atmospheric sciences from Yonsei University, Seoul, South Korea, in 2018, where he is currently pursuing the Ph.D. degree.

His research primarily focuses on the sensitivity of microwaves to the microphysical characteristics of hydrometeors. In addition, he is investigating the dynamic phenomena shown by satellite latent heating estimation.